J. Fluid Mech. (1994), *vol.* 262, *pp.* 293–324

Convection in a rotating cylinder. Part 2. Linear theory for low Prandtl numbers

By H. F. GOLDSTEIN[1], E. KNOBLOCH[1], I. MERCADER AND M. NET[2]

[1] Department of Physics, University of California, Berkeley, CA 94720, USA

[2] Departament de Física Aplicada, Universitat Politècnica de Catalunya, E 08034 Barcelona, Spain

(Received 23 February 1993 and in revised form 13 September 1993)

The onset of convection in a low-Prandtl-number fluid confined in a uniformly rotating vertical cylinder heated from below is studied. The linear stability problem is solved for perfectly conducting stress-free or rigid boundary conditions at the top and bottom; the sidewalls are taken to be insulating and rigid. For these Prandtl numbers axisymmetric overstability leads to an oscillating concentric pattern of rolls. When the instability breaks axisymmetry the resulting pattern must in addition precess. The relationship between these two types of oscillatory behaviour is explored in detail. The complex interaction between different types of neutrally stable modes is traced out as a function of the Prandtl and Taylor numbers, as well as the aspect ratio. A qualitative explanation is provided for the multiplicity of modes of a given azimuthal wavenumber and its dependence on the parameters. Specific predictions are made for the Prandtl numbers 0.025, 0.49 and 0.78, corresponding to mercury, liquid helium 4 and compressed carbon dioxide gas.

1. Introduction

In a recent paper Goldstein *et al.* (1993) presented a detailed solution of the linear stability problem describing the onset of convection in a uniformly rotating right circular cylinder heated from below. The computations undertaken by Goldstein *et al.* were motivated by a recent experiment of Zhong, Ecke & Steinberg (1991, 1993) using water as the experimental fluid. These experiments revealed that the conduction state loses stability to non-axisymmetric modes that precess counter to the direction of rotation. That non-axisymmetric patterns should precess is an immediate consequence of the SO(2) symmetry of the system (Ecke, Zhong & Knobloch 1992). An unexpected result of the calculations was the discovery of two quite distinct modes of instability. The first type, called a body mode, is a convective mode of the type that are present in a non-rotating cylinder (Marqués *et al.* 1993). These modes fill the interior of the container, and have low amplitude near the wall. If they break axisymmetry they precess, albeit slowly. The second type of mode, called a wall mode, is confined to the vicinity of the sidewall, and precesses much more rapidly. It is always non-axisymmetric. The existence of these modes was anticipated by Buell & Catton (1983) although their precession was not. Which mode is the one that first becomes unstable as the Rayleigh number is increased depends on the parameters of the system: the rotation rate measured by Taylor number $\mathcal{T}^2$, the aspect ratio Γ of the cylinder and of course the Prandtl number σ. The calculated critical Rayleigh numbers, precession

frequencies and selected azimuthal wavenumbers for $\sigma = 6.8$ and $\Gamma = 1$ and 2.5 agree very well with the observations, as documented in Goldstein *et al.* (1993) and Zhong *et al.* (1993).

The experiments hitherto performed have always been operated in the regime where the wall modes are the preferred mode of instability. The calculations of Goldstein *et al.* (1993) show, however, that body modes are preferred for sufficiently low rotation rates and sufficiently large aspect ratios. As the rotation rate increases (or the aspect ratio decreases) they are superseded by the wall modes. A significant aspect of the work of Goldstein *et al.* (1993) concerns the infinite aspect ratio limit of their calculations. Here it is found that it is the body modes that approach the results obtained by Chandrasekhar (1961) for an unbounded layer in the sense that the critical Rayleigh number approaches that computed by Chandrasekhar, while the precession frequency tends (in an oscillatory manner) towards zero, as the aspect ratio increases. Another way to look at Chandrasekhar's result is as an approximation to the result for an axisymmetric roll pattern. As already mentioned such patterns do not precess, and are necessarily body modes; their critical Rayleigh number as a function of the rotation rate follows the Chandrasekhar result quite closely. The bifurcation to such modes is of course a steady-state one, in contrast to the bifurcation to non-axisymmetric modes which becomes a Hopf bifurcation as a result of the broken reflection symmetry in vertical planes (Ecke *et al.* 1992).

The results for the unbounded layer show that for sufficiently small Prandtl numbers ($\sigma < 0.68$) and large enough rotation rates the initial instability takes the form of overstable oscillations (Chandrasekhar 1961; Clune & Knobloch 1993). One expects, therefore, that in a cylinder the bifurcation to axisymmetric rolls will also be a Hopf bifurcation for sufficiently low Prandtl numbers. In the nonlinear regime this bifurcation leads to either axisymmetric standing waves or travelling waves that propagate in the radial direction (Clune & Knobloch 1993), in contrast to the Hopf bifurcation for non-axisymmetric modes which gives rise to patterns that precess in the azimuthal direction. In this paper we verify the above hypothesis, and determine what happens to the overstable modes when the preferred mode is non-axisymmetric. Generic theory predicts that the initial instability remains a Hopf bifurcation, and that it gives rise to a precessing pattern just as for large Prandtl numbers. How the low-Prandtl-number character of the modes manifests itself, and how the transition from radial oscillations to precessing oscillations takes place remain unanswered by such a theory.

In the present paper we therefore examine the linear stability problem describing the onset of convection in a rotating cylinder for small Prandtl numbers. We study the problem both with stress-free boundary conditions at the top and bottom, and with no-slip boundary conditions. In the following we refer to these as the stress-free and rigid problems, respectively. The boundary conditions on the curved sidewall are no slip in both cases. For comparison with experiments we use fixed temperature boundary conditions at the top and bottom, and insulating ones on the sides. The problems are solved as in Goldstein *et al.* (1993).

The paper is somewhat in the spirit of a related study of the onset of low-Prandtl-number convection in rotating spheres by Zhang & Busse (1987) in that we attempt to explain the various features of the linear stability problem as the Prandtl number decreases. However, because of the simpler geometry, we are able to provide a more detailed discussion, and as a result uncover behaviour that is more complex than in the problem studied by Zhang & Busse (1987).

In §2 we briefly summarize the basic equations. In §3 we present the results for the

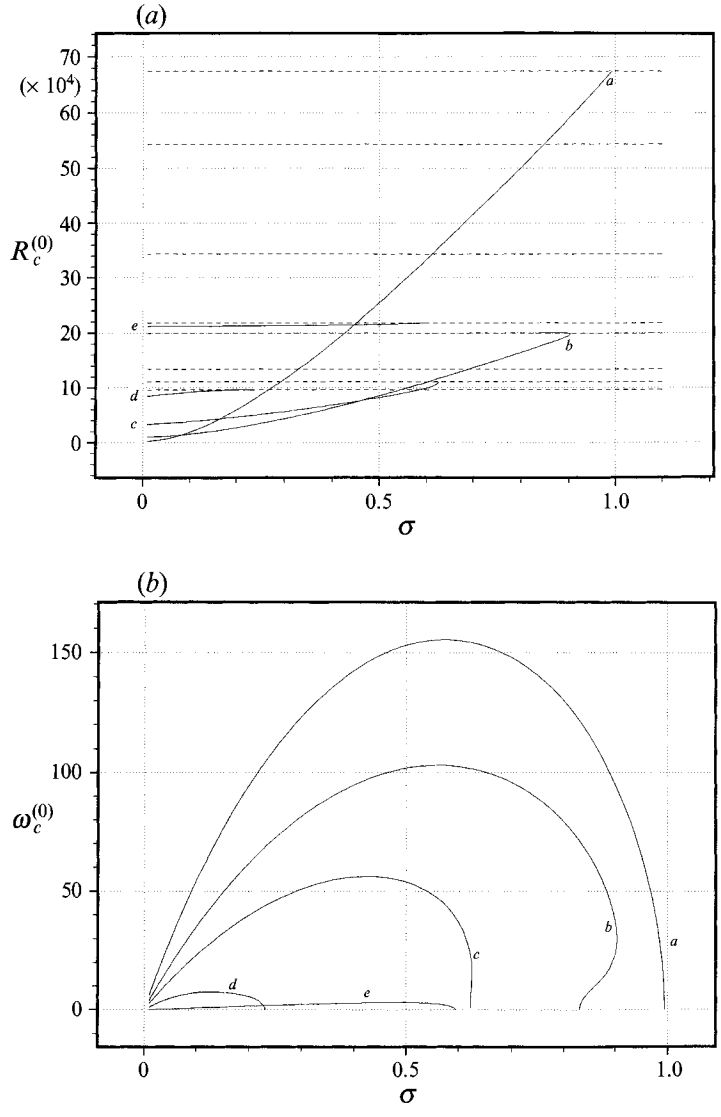

FIGURE 1. (*a*) The critical Rayleigh number $R_c^{(0)}$ and (*b*) the corresponding oscillation frequency $\omega_c^{(0)}$ for axisymmetric modes as a function of the Prandtl number in a $\Gamma = 1$ cylinder. The rotation rate is specified by the square root of the Taylor number, $\mathscr{T} = 1000$. The dashed lines correspond to steady modes ($\omega_c^{(0)} = 0$) and are independent of σ. The solid lines correspond to oscillatory modes. The correspondence between the frequencies and critical Rayleigh numbers is indicated by the letters *a*, *b*, ... The full spectrum of oscillatory modes is found by reflecting figure (*b*) in the $\omega = 0$ axis. The points where the oscillation frequency vanishes are Takens–Bogdanov points.

stress-free case, for which essentially exact solutions can be obtained. Consequently we have used this case to elucidate the complexity of the modal structure present at low Prandtl numbers. In §4 we explain a number of qualitative aspects of the results, emphasizing in particular the high multiplicity of modes with the same azimuthal wavenumber that exist for fixed values of the aspect ratio and the rotation rate at low Prandtl numbers. To understand the origin of such complexity we trace the Prandtl-number and Taylor-number dependence of the modes as well as their aspect-ratio dependence, emphasizing the fate of the wall modes as the Prandtl number decreases.

In §5 we present the corresponding results for the rigid case, and interpret the results on the basis of our experience with the stress-free case. These results, which focus on the critical Rayleigh numbers, precession frequencies and selected azimuthal wavenumbers are obtained for Prandtl numbers and aspect ratio for existing experiments on convection in liquid helium above the λ point for which $\sigma = 0.49$ (Lucas, Pfotenhauer & Donnelly 1983; Pfotenhauer, Lucas & Donnelly 1984; Pfotenhauer, Niemela & Donnelly 1987) and for dilute ^{3}He–^{4}He mixtures for which $\sigma = 0.525$ (Thurlow 1993). Some results for the Prandtl number of mercury ($\sigma = 0.025$) and for proposed experiments on compressed carbon dioxide gas ($\sigma = 0.78$) are also presented. Section 5 concludes with a comparison of the results with the experiments. A brief discussion follows in §6.

2. The equations

We consider Boussinesq convection in a vertical right circular cylinder of radius d and height h, filled with a pure fluid and rotating with constant and uniform angular velocity Ω about its axis. We denote by Γ its aspect ratio d/h. The linearized, non-dimensionalized equations of motion take the form (Chandrasekhar 1961)

$$(\sigma^{-1}\partial_t - \nabla^2)\boldsymbol{u} = -\nabla p + R\Theta\hat{\boldsymbol{z}} + \mathcal{T}\boldsymbol{u}\times\hat{\boldsymbol{z}}, \tag{1}$$

$$(\partial_t - \nabla^2)\Theta = w, \tag{2}$$

$$\nabla\cdot\boldsymbol{u} = 0, \tag{3}$$

where $\boldsymbol{u} = u\hat{\boldsymbol{r}} + v\hat{\boldsymbol{\phi}} + w\hat{\boldsymbol{z}}$ is the velocity field, Θ and p are the departures of the temperature and pressure from their conduction profiles, and $\hat{\boldsymbol{z}}$ is the unit vector in the vertical direction. The quantities $\mathcal{T} \equiv 2\Omega h^2/\nu$, $R \equiv g\alpha\Delta T h^3/\kappa\nu$, and $\sigma \equiv \nu/\kappa$ denote, respectively, the square root of the Taylor number, the Rayleigh number, and the Prandtl number. In these equations, length is in units of the layer thickness, h, and time is in units of the vertical thermal diffusion time, h^2/κ. This non-dimensionalization is retained in order to connect the low-Prandtl-number results obtained here with those of Goldstein *et al.* (1993). In writing (1) we have assumed that the Froude number $d\Omega^2/g$ is sufficiently small that the buoyancy force continues to act in the vertical direction.

In the following we use two types of boundary conditions. The boundary conditions for the problem we call stress free are

$$\partial_z u = \partial_z v = w = \Theta = 0 \quad \text{on} \quad z = 0, 1, \tag{4}$$

$$u = v = w = \partial_r \Theta = 0 \quad \text{on} \quad r = \Gamma, \tag{5}$$

and correspond to free-slip, impenetrable, infinitely conducting horizontal plates at top and bottom, and a rigid, impenetrable, insulating sidewall. Those for the rigid problem are

$$u = v = w = \Theta = 0 \quad \text{on} \quad z = 0, 1, \tag{6}$$

$$u = v = w = \partial_r \Theta = 0 \quad \text{on} \quad r = \Gamma, \tag{7}$$

and correspond to rigid (i.e. no-slip) boundaries everywhere. In the following we refer to these as boundary conditions A and B, respectively.

The conduction solution, $u = v = w = \Theta = 0$, is stable to small perturbations below some critical value of the Rayleigh number, R_c, which depends, in general, on the

aspect ratio, the Taylor number, and the Prandtl number, as well as the boundary conditions. Thus, if we write the time dependence of a solution to the linear problem as e^{st}, then $Re(s) < 0$ for all solutions when $R < R_c$. At $R = R_c$ there is for the first time a neutrally stable solution to the linear problem, i.e. $\mathrm{Re}(s) = 0$. If $\mathrm{Im}(s) = 0$, the bifurcation is steady-state, and if $\mathrm{Im}(s) = \omega_c \neq 0$, we have a Hopf bifurcation with Hopf frequency ω_c. In the following we use the notation $R_c^{(m)}$ and $\omega_c^{(m)}$ to denote the values of R_c and ω_c for a mode with azimuthal wavenumber m. The resulting values of $R_c^{(m)}$ can be minimized with respect to m to determine the azimuthal wavenumber of the mode that sets in first. The resulting critical Rayleigh number and the corresponding frequency will be denoted by R_c and ω_c with no superscript. As already mentioned the critical mode may be a body mode or a wall mode, depending on parameters. For moderate Prandtl numbers the distinction between these modes is unambiguous. We shall see below that for low Prandtl numbers this is no longer so.

3. Results for the stress-free case

We use the boundary conditions A to elucidate both the parameter dependence and multiplicity of the solutions to the linear stability problem. With these boundary conditions the stability problem is separable (e.g. $\Theta(r, \phi, z, t) = A(r)\, e^{im\phi + i\omega t} \sin n\pi z$); all the results reported below are for the fundamental wavenumber $n = 1$ in the vertical. In order to relate the results to the moderate-Prandtl-number results of Goldstein *et al.* (1993) we choose $\Gamma = 1$ and $\mathscr{T} = 1000$. We begin by describing the results for $m = 0$ corresponding to axisymmetric instability. Figure 1 (*a*) shows $R_c^{(0)}$ as a function of σ. There are two types of curves. The dashed lines, showing the threshold Rayleigh number for steady modes, are Prandtl number independent. The solid curves indicate the onset of overstability. These curves extend from $\sigma = 0$ to a termination point on one of the dashed curves. This termination point is called the Takens–Bodganov point (hereafter TB point) and will be discussed in greater detail in §4 below. Note that when the overstable solutions exist they set in with a lower Rayleigh number than the corresponding steady state, as in other systems of this type (see, for example, Da Costa, Knobloch & Weiss 1981). Not all of the steady modes have TB points associated with them, however. Figure 1 (*b*) shows the corresponding frequencies as a function of σ. The various curves are labelled to indicate the correspondence. The oscillation frequency in all cases increases with the Prandtl number before decreasing again to zero at the TB point. Since the oscillations are axisymmetric the dispersion relation determining the frequencies is even in ω; consequently for each $\omega > 0$ shown there is a corresponding negative ω as well, with the same critical Rayleigh number. The complete frequency spectrum is therefore obtained by reflecting figure 1 (*b*) in $\omega = 0$. In the following we refer to these modes as inertial oscillations since the restoring force is provided by the Coriolis force.

Figure 2 shows the corresponding results for $m = 1$ modes. These modes break the axisymmetry of the system since they are no longer invariant under rotations, i.e. a rotation applied to an $m = 1$ solution yields a new and distinct solution as opposed to the same solution. The $m = 1$ modes break axisymmetry the least, however, and the results of figure 2 therefore bear some resemblance to those shown in figure 1. This is best seen in figure 2 (*b*), which shows how the frequency spectrum becomes asymmetric with respect to reflection in $\omega = 0$ as soon as the modes become non-axisymmetric. Specifically, there are now no modes with zero frequency. The steady modes present for $m = 0$ for Prandtl numbers above the TB point now connect smoothly with the positive frequency oscillatory modes for lower Prandtl numbers, while the steady modes

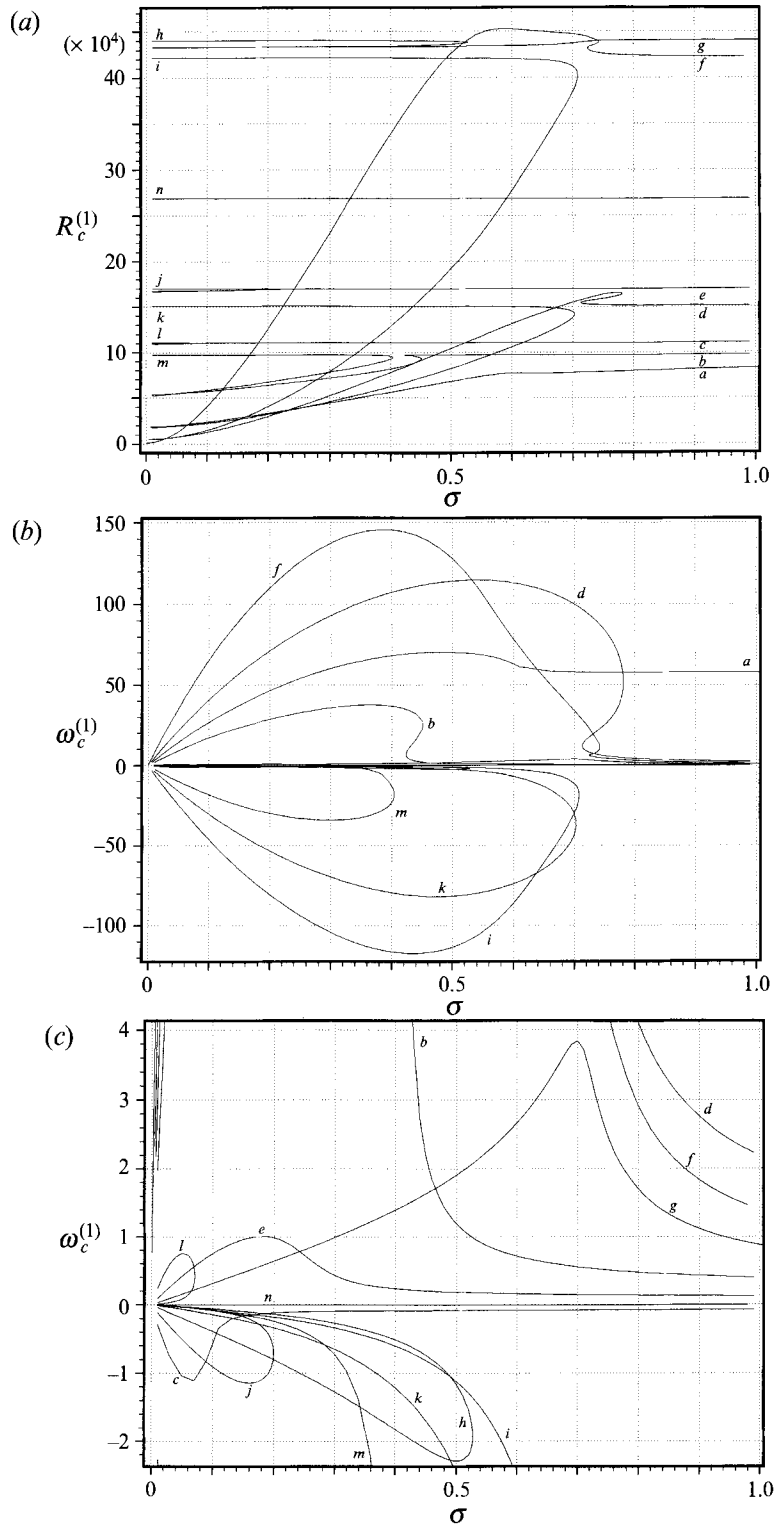

FIGURE 2. As for figure 1, but for $m = 1$ modes. All bifurcations are now oscillatory and produce precessing modes. The mode a is the wall mode of Goldstein *et al.* (1993). (*c*) A detail of (*b*) for lower frequencies. The modes are corotating when $\omega_c^{(1)} < 0$ and counter-rotating when $\omega_c^{(1)} > 0$.

present for Prandtl numbers smaller than the TB point connect with the negative frequency oscillatory modes. Thus the broken axisymmetry causes the steady modes for large Prandtl numbers to precess in the retrograde direction ($\omega > 0$) while those at small Prandtl numbers precess in the prograde direction ($\omega < 0$). As the Prandtl number decreases, the precession frequency of the retrograde mode increases slowly until the vicinity of the corresponding TB point where it begins to increase abruptly reaching values of the order of the corresponding $m = 0$ mode, before once again decreasing to zero. Similar behaviour occurs for the prograde modes with increasing Prandtl number. We refer to those modes that arise as perturbations of axisymmetric oscillations as inertial modes, with those arising as perturbations of steady modes referred to as convective modes. Note that as a function of the Prandtl number a mode can change from inertial to convective or vice versa.

As a consequence of the relation of figure 2(*b*) to figure 1(*b*) it is a simple matter to pair up the different frequency curves in figure 2(*b*): *b* goes with *m*, *d* goes with *k*, and *f* goes with *i*, in the sense that they arise from the breakup of the same $m = 0$ modes. Additional $m = 1$ modes can be seen in figure 2(*c*). Notice, however, that there is a single positive frequency mode, labelled *a*, that has no counterpart with $\omega < 0$. This mode, unlike for example the modes *d* and *f*, has a substantial precession frequency for large Prandtl numbers, suggesting that it is a wall mode, in the terminology of Goldstein *et al.* (1993). Figure 3(*a*) demonstrates that this is indeed so. The figure shows the vertical velocity eigenfunction at mid-level, $w(r, 0, \frac{1}{2})$, as a function of r for this mode. For non-axisymmetric modes this eigenfunction vanishes both at the origin and at the wall. For large Prandtl numbers the eigenfunction peaks near the wall, while the amplitude in the body of the container is small. This is in contrast to the slowly precessing modes *d* and *f* which fill the whole container but have a small amplitude near the wall. However, as the Prandtl number decreases, the structural difference between the two types of modes is gradually lost.

Figure 3(*a*) shows that the outer peak of the vertical velocity $w(r, 0, \frac{1}{2})$ for mode *a* decreases while the inner one increases, so that by the time $\sigma = 0.4$ mode *a* looks indistinguishable from mode *b*. The change in *a* is most abrupt near $\sigma = 0.62$, where the frequency of *a* undergoes the fastest change (see figure 2*b*). This change in the character of the eigenfunction is quantified in figure 3(*b*) which shows the ratio α of the first minimum (near $r = 0$) to the second minimum (near $r = \Gamma$) as a function of σ. This change of character should not come as a surprise since the wall mode is likely to be a convectively destabilized Poincaré mode of the rotating cylinder. This identification of the wall modes with Poincaré modes is supported not only by their spatial structure but also by their absence in the axisymmetric case, and will be explored in detail elsewhere. The wall modes are thus likely to be inertial modes as well, the main difference between these two types of inertial oscillation resting in the fact that the wall modes owe their existence to the sidewall while the low-Prandtl number oscillations do not. In the following we shall continue to refer to mode *a* as a wall mode, its change of character at small σ notwithstanding.

Figure 2(*a*) shows the critical Rayleigh numbers corresponding to figure 2(*b*). Observe that the transition from the 'steady' to the 'oscillatory' mode as a function of the Prandtl number is characteristically accompanied by a fold in the critical curve of the retrograde mode. Not all the mode interactions take this form, however. Some, specifically the interactions between *c* and *l*, *e* and *j*, and *g* and *h*, take a somewhat different form: here the reconnection still occurs as described above, but the fold is absent. An explanation of the qualitative aspects of these mode interactions can be found in §4. Note also that among the $m = 1$ modes the wall mode *a* is preferred for

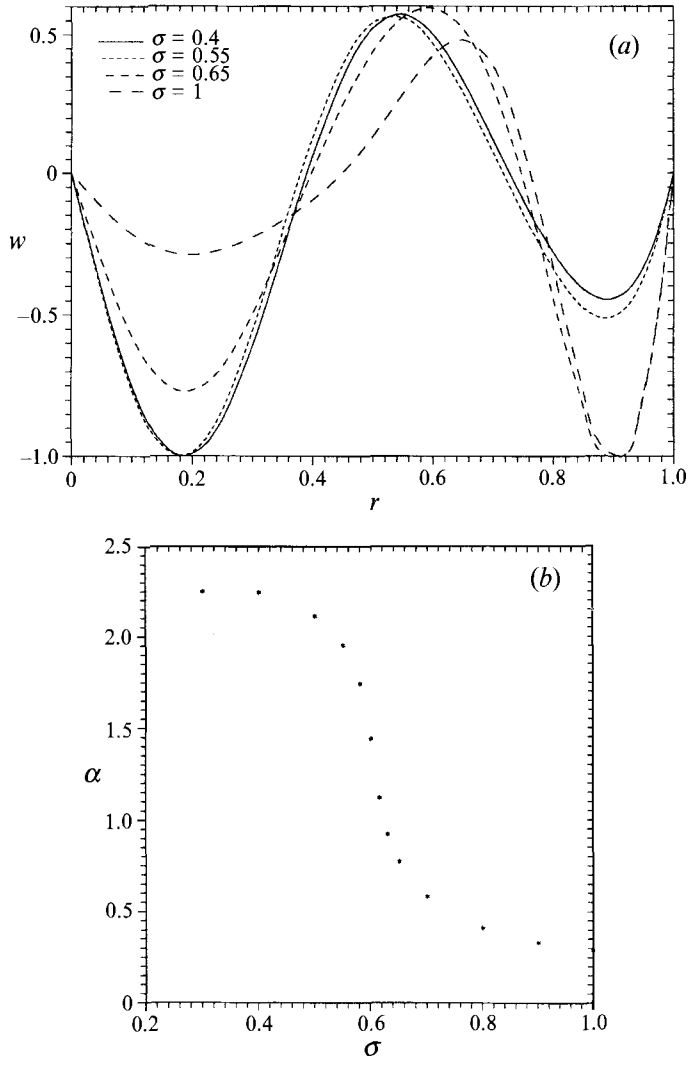

FIGURE 3. (*a*) The eigenfunction $w(r, 0, \frac{1}{2})$ for the wall mode *a* for several values of the Prandtl number. The global minimum has been scaled to -1 in all cases. (*b*) The ratio α of the first minimum (near $r = 0$) to the second minimum (near $r = \Gamma$) as a function of the Prandtl number, showing the rapid change in the eigenfunction near $\sigma = 0.62$.

$\sigma > 0.25$, but that for smaller σ it is briefly superseded by the prograde k mode and then for $0.227 > \sigma > 0.044$ by the retrograde mode d. For yet smaller σ the mode i has the least Rayleigh number, while for $\sigma < 0.032$ f dominates. These results indicate how sensitive the mode selection process is to the exact value of the Prandtl number when it is small. In particular a mode preferred at low Prandtl number like f may have a huge critical Rayleigh number by the time σ has increased to 0.5. Thus the modes relevant at small Prandtl numbers may bear no resemblance to those at larger σ. Notice also that there are some aspects of figure 2(*a*) that are not visible in figure 2(*b*). This is the sequence of mode pairings with decreasing Prandtl number: for $\sigma < 0.25$ mode a pairs up with k, with d remaining unpaired, while for $\sigma < 0.044$ d pairs up with i, with f unpaired. We discuss the origin of this behaviour in §4.

Figure 1 reveals an interesting and important feature: axisymmetric oscillatory

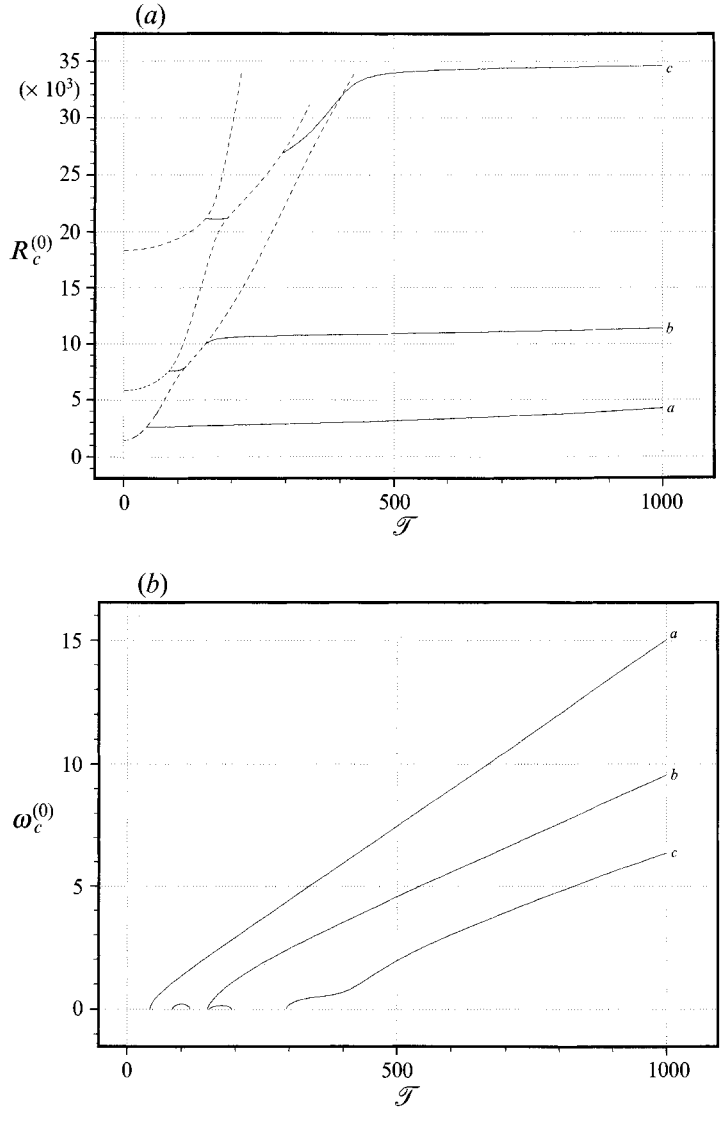

FIGURE 4. As for figure 1, but showing the dependence of (*a*) $R_c^{(0)}$ and (*b*) $\omega_c^{(0)}$ on $\mathscr{T}$ for the $m = 0$ modes when $\sigma = 0.025$, $\Gamma = 1$. The modes labelled *a*, *b*, *c* correspond to those shown in figure 1. Note in particular the connections between different steady-state modes via oscillatory modes and their manifestation in (*b*).

convection appears to be possible for all $\sigma < 1$, although for the larger values of σ it may be preceded by a transition to a steady axisymmetric mode. In an unbounded layer with free boundaries at the top and bottom Chandrasekhar (1961) showed that oscillations disappear when $\sigma > (2/3)^{\frac{1}{2}}$. This limit is approached in the limit of large rotation rates and applies to rigid boundaries as well (Clune & Knobloch 1993). The difference between the bounded and unbounded problems appears at first sight to be surprising. However, the unbounded result is obtained by minimizing the critical Rayleigh number for the onset of overstability over all horizontal wavenumbers. In a finite container this procedure is not available: the horizontal structure is now fixed by the boundary. Indeed if one re-examines the theory for the unbounded layer, one finds

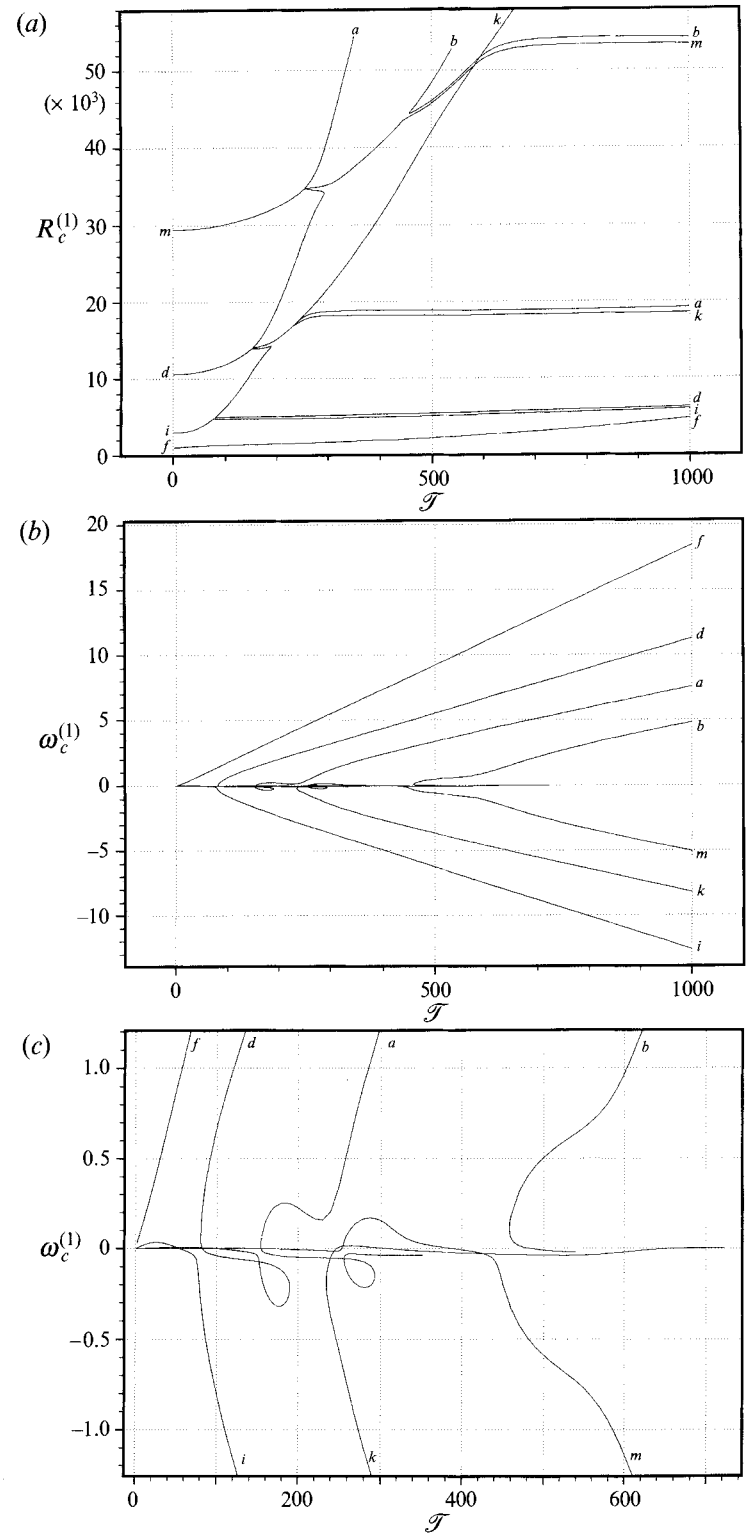

FIGURE 5. As for figure 4, but for $m = 1$ modes. All bifurcations are now oscillatory and produce precessing modes. (*c*) A detail of (*b*) showing the loops in modes *d* and *a* created from the ovals in figure 4(*b*).

that for a fixed wavenumber the maximum value of the Prandtl number at which oscillations can occur is once again unity.

We now turn to the Taylor-number dependence of the above results, with a particular emphasis on the fate of the various types of modes as the rotation rate is reduced. We choose $\sigma = 0.025$, and present results as a function of the Taylor number $\mathscr{T}$ for both $m = 0$ and $m = 1$. The aspect ratio is kept at $\Gamma = 1$.

We begin by showing the case $m = 0$ (see figure 4). For $\sigma < 1$ the Taylor number must exceed some minimum value that depends on σ (the TB point) before overstable axisymmetric modes become possible. There are two types of such TB points, those that give rise to oscillations whose frequency increases monotonically with $\mathscr{T}$, and those that connect back to another TB point. Figure 4(*a*) shows that the former correspond to the oscillations one expects at larger rotation rates by analogy with the unbounded problem; these modes correspond to the modes *a*, *b* and *c* already shown in figure 1. The latter are associated with Hopf curves that connect different steady modes. Notice the deformation of the steady-state neutral curves in the vicinity of these connections. The behaviour seen here differs significantly from the unbounded system where exactly one TB point exists on each steady mode. As in figure 1(*b*) the complete spectrum of oscillation frequencies is obtained by reflecting figure 4(*b*) in $\omega = 0$. When this is done the Hopf curves connecting steady-state neutral curves produce disconnected ovals. The deformation of $\omega_c^{(0)}$ for mode *c* seen in figure 4(*b*) suggests that these ovals are created by a pinching-off process as parameters are varied. This process allows a large-$\mathscr{T}$ oscillatory mode to change the steady-state mode on which it terminates, and leaves behind a short segment of oscillations connecting the two steady-state modes involved (cf. figure 4*a*). Figure 5(*a*) shows the corresponding results for $m = 1$. The seven modes that are visible in figure 2(*a*) at $\sigma = 0.025$ are now at the right of the figure at $\mathscr{T} = 1000$. The figure shows that for non-axisymmetric modes the rotation of the container splits the neutral stability curves for all the oscillatory $m = 0$ modes. This rotational splitting is expected on general grounds (cf. Knobloch 1992), and arises because prograde ($\omega < 0$) and retrograde ($\omega > 0$) modes no longer couple to the rotation in the same way. As a result one or other type of mode comes in first. In the present case the prograde mode always has the lower critical Rayleigh number at large $\mathscr{T}$. The difference between the prograde and retrograde modes can also be seen in the asymmetry of the frequency spectrum with respect to reflection in $\omega = 0$ (figure 5*b*). Thus it is the rotational splitting of the modes *a*, *b* and *c* in figure 4(*a*) that is responsible for the modes (d, i), (a, k) and (b, m) in figure 5(*a*), respectively. Figure 5(*a*) reveals, however, the presence of an extra mode at larger $\mathscr{T}$, labelled *f*. This mode does not originate through rotational splitting; it has no (nearly) symmetric counterpart in figure 5(*b*) and its precession frequency decreases linearly to zero with decreasing $\mathscr{T}$. It is also the preferred mode in the range of $\mathscr{T}$ shown. The existence of such a mode is in accord with general considerations (Ecke *et al.* 1992). Since this mode does not appear to have an axisymmetric counterpart we identify it as a wall mode of the rotating cylinder, in contrast to the other modes (d, i, a, k, b, m) which are non-axisymmetric counterparts of the usual oscillatory modes. Note that this identification is supported both by the relatively high precession frequency of the mode (see figure 5*b*), and by the fact that this precession is counter to the direction of rotation ($\omega > 0$).

We discuss next the effect of non-axisymmetry on the transition between steady and oscillatory modes. Recall first that generically the bifurcation to a non-axisymmetric mode cannot be stationary. Consequently all the curves in figure 5(*a*) correspond to

Hopf bifurcations. This is clearly seen in figure 5(*a*) at small $\mathscr{T}$ where the neutral stability curves for steady-state bifurcations shown in figure 4(*a*) are seen to have unambiguous Hopf counterparts. In the following we characterize the modes as prograde or retrograde depending on whether $\omega < 0$ or $\omega > 0$ at large ω. With increasing $\mathscr{T}$ one sees two types of interaction between the Hopf curves that arise from the steady and oscillatory neutral stability curves upon considering non-axisymmetric states. One type of interaction is organized around the TB points, and results in what we call 'mode repulsion', as in the interaction between modes (i, d) near $\mathscr{T} = 80$, between modes (k, a) near $\mathscr{T} = 240$ and between modes (m, b) near $\mathscr{T} = 450$. Note that the interaction near $\mathscr{T} = 240$ is of the same type as the other two, except for the fact that it is the mode k, i.e. the prograde mode, that turns around, and not the retrograde mode. This type of interaction comes about because of the rotational splitting of the Hopf curves for non-axisymmetric modes, and will be discussed in more detail in §4. The other type of interaction comes about through the rotational splitting of the Hopf curves connecting the steady-state neutral curves in the axisymmetric case, and results in either *crossing* or an *avoided crossing* of the corresponding non-axisymmetric Hopf curves. Examples of the former are found near $\mathscr{T} = 255$, and of the latter near $\mathscr{T} = 154$ (see figure 5*a*). Both interactions are of the same type except for the fact that in the latter case the interaction takes place between two retrograde modes (modes *a* and *d* both precess counter to the direction of rotation at large $\mathscr{T}$), while in the former it takes place between a retrograde mode (mode *a*) and a prograde one (mode *m*).

Figure 5(*b*) shows the corresponding precession frequencies as a function of $\mathscr{T}$, with a blow up shown in figure 5(*c*). Observe first that, with the exception of the inertial mode *f*, all the modes change their direction of precession as a function of $\mathscr{T}$. Consequently it *is* possible for a non-axisymmetric mode to be stationary (cf. Bestehorn *et al.* 1992), although the situation is non-generic in the sense that a small change in parameters will make the mode precess again. Observe next that the seven TB points depicted in figure 4(*b*) break up in a characteristic fashion when $m = 1$. As already mentioned, the frequency spectrum loses its symmetry about $\omega = 0$, and the frequencies of the prograde and retrograde modes disconnect (see the interaction between the modes (i, d), (k, a) and (m, b)), exhibiting the mode repulsion already observed in figure 5(*a*). The detail shown in figure 5(*c*) shows why the (k, a) interaction at $\mathscr{T} = 240$ differs from those at $\mathscr{T} = 80$ and 450; the modes *a* and *k* are turned by their repulsion in opposite directions from those of the corresponding modes in the other two interactions. The 'generic' situation is illustrated by the (m, b) interaction in which *m* and *b* connect to $\omega = 0$ as $\mathscr{T} \to 0, \infty$, respectively. In contrast the modes (i, d) both ultimately connect to $\omega = 0$ as $\mathscr{T} \to 0$, while (k, a) connect to $\omega = 0$ as $\mathscr{T} \to \infty$. There are thus a number of modes that are not connected to $\mathscr{T} = 0$, i.e. these modes have no counterpart in the non-rotating system. In order for this to be possible one or other of the interacting modes must turn around, and this process involves the appearance of the prominent loops in figure 5(*c*). These loops arise from the reconnection of the ovals in figure 4(*b*) to the oscillations arising from the steady state in figure 4, the loop in *d* coming from the first oval in figure 4(*b*), while that in *a* comes from the second one. For example, the avoided crossing near $\mathscr{T} = 154$ (see figure 5*a*) comes about through the repulsion of the modes *d* and *a*. It is this interaction that deflects *a* back towards larger $\mathscr{T}$ and *d* towards smaller $\mathscr{T}$, and hence is responsible for the behaviour of the modes (i, d) as $\mathscr{T} \to 0$ and of (k, a) as $\mathscr{T} \to \infty$. In this process *a* undergoes a further interaction, this time with the mode *m*, but without an overall change in direction; this is accomplished by means of the loop to the right of the

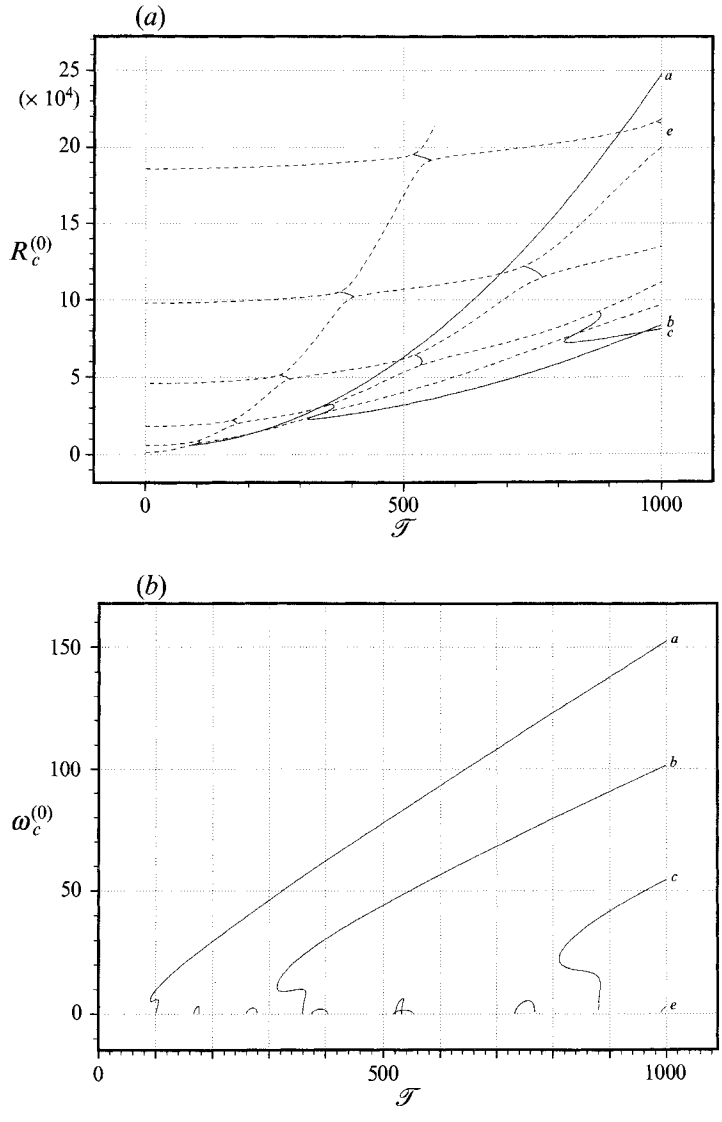

FIGURE 6. As for figure 4, but for $\sigma = 0.49$.

interaction point ($\mathscr{T} = 255$), and results in the mode crossing seen at the corresponding point in figure 5(*a*). The overall effect of these interactions is to prevent mode *a*, the large-Prandtl-number wall mode, from reaching $\mathscr{T} = 0$ as befits a mode tentatively identified as an inertial mode. But the manner in which *a* is turned around is remarkably complex, involving a high multiplicity of modes near particular values of the rotation rate.

The results presented above for fixed $\mathscr{T}$ and variable σ are related to those for fixed σ and variable $\mathscr{T}$. For example, the turning point in mode *d* near $\mathscr{T} = 80$ when $\sigma = 0.025$ comes about when a loop of the form of that labelled *l* in figure 2(*c*) first cuts the line $\sigma = 0.025$. This first occurs as $\mathscr{T}$ increases through $\mathscr{T} = 80$. Thus, increasing $\mathscr{T}$ is equivalent to decreasing σ and much of the structure seen in figures

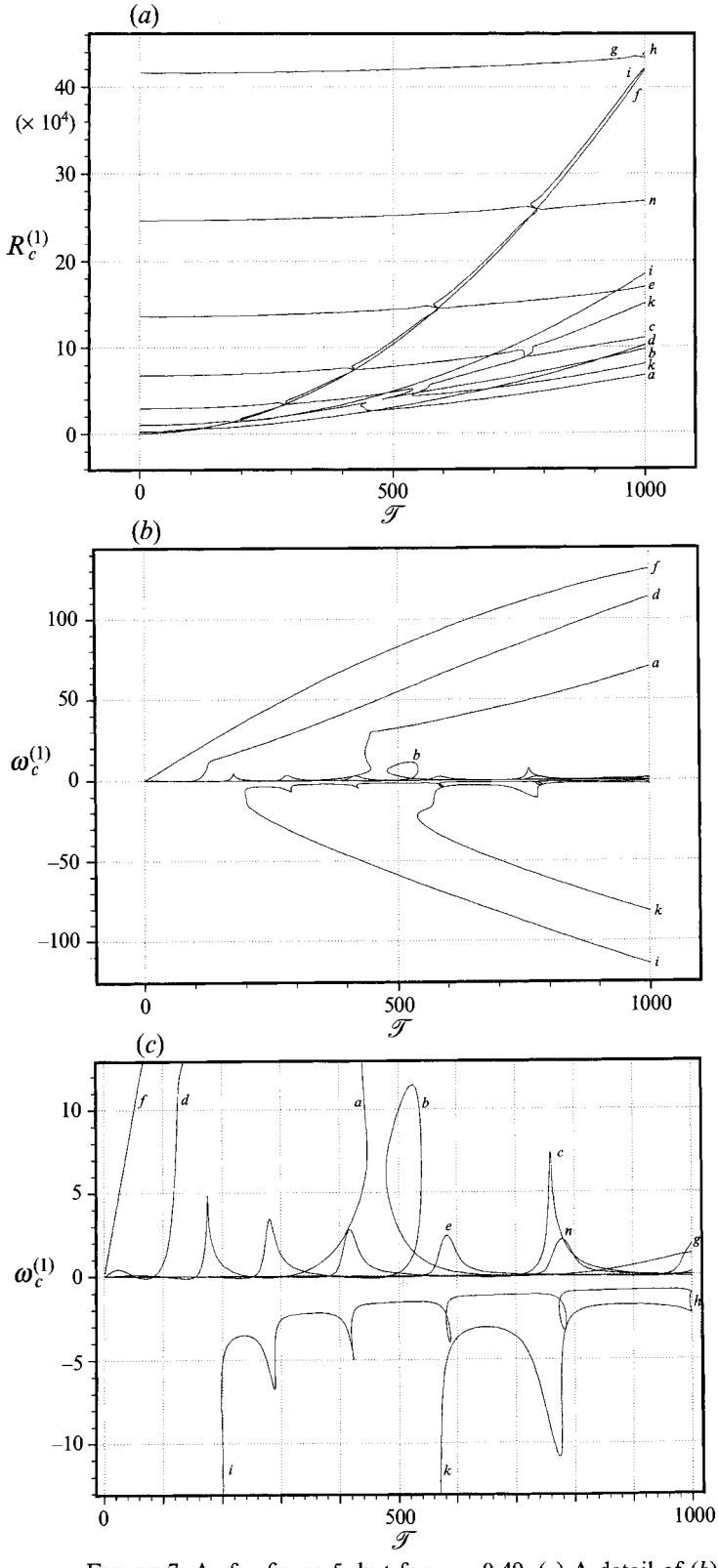

FIGURE 7. As for figure 5, but for $\sigma = 0.49$. (*c*) A detail of (*b*).

2(*b*) and 5(*b*) can be related this way. In particular the (*i*, *d*) mode interaction moves to lower σ as $\mathscr{T}$ decreases, while at fixed $\mathscr{T}$ increasing σ results in a loss of modes two at a time.

We may summarize the behaviour shown in figure 5 as follows. Recall that at $\mathscr{T} = 1000$ (see figure 2) modes *f* and *i* arise from the breakup of a pair of $m = 0$ modes, and so do *d* and *k*, and *b* and *m*. With decreasing $\mathscr{T}$ the pairing shifts. The mode *f* becomes unpaired while the remaining modes pair up, *d* with *i*, and *a* with *k*. As a consequence the unpaired mode *a* exchanges its role with the mode *f*. This mode is a steady $m = 1$ mode of the non-rotating cylinder; when the cylinder begins to rotate the mode begins to precess as described by Ecke *et al.* (1992). It is of interest that the rate of precession of this mode is soon similar to that of, for example, the modes *d* and *i*, which are created in the splitting of a pair of *oscillatory* $m = 0$ modes.

It is interesting to compare the above results for $\sigma = 0.025$ with those for an intermediate value of the Prandtl number: $\sigma = 0.49$. This case is perhaps the most complicated of all. As before we begin with the $m = 0$ modes and show in figure 6 the critical Rayleigh numbers and oscillation frequencies of the low-lying modes. The number of oscillatory modes connecting the steady modes is now much larger, and there may be several connections between the same steady states (see figure 6*a*). In addition the large-$\mathscr{T}$ oscillatory modes terminate on the steady-state modes with a pronounced fold. We have checked that these folds develop continuously from the situation depicted in figure 4(*a*) as the Prandtl number is raised. In consequence the frequencies $\omega_c^{(0)}$ also develop folds, and these form through a reconnection between the ovals shown in figure 4(*b*) and the Hopf curves extending to large $\mathscr{T}$. Of course other mode interactions create new segments of Hopf curves, responsible for the new ovals in figure 6(*b*). Figure 7 shows the corresponding results for $m = 1$ modes. This figure exhibits similar phenomena to those discussed in connection with figure 5(*b*, *c*), except that the modal structure is yet more complex. The typical mode interaction now results in mode crossing (see figure 7*a*). The new mode this time is the one that appears to pass directly through a number of these mode crossings. This mode connects smoothly to zero rotation rate (figure 7*b*) and is the preferred mode from among the $m = 1$ modes for $\mathscr{T} < 126$. Mode *a*, the wall mode at large Prandtl numbers, is preferred for $\mathscr{T} > 460$ and is now also connected to $\mathscr{T} = 0$, in contrast to the situation for $\sigma = 0.025$. It follows that somewhere in $0.025 < \sigma < 0.49$ mode *a* must cease to be connected to $\mathscr{T} = 0$. How this takes place remains unclear. Figure 7(*c*) shows a detail of some of the large number of cusps and loops that some of the modes go through in the process of turning around to large $\mathscr{T}$.

We examine, finally, in figures 8 and 9 the behaviour of the modes with increasing aspect ratio Γ for $\sigma = 0.49$ and $\mathscr{T} = 1000$. Figure 8(*a*) shows the results for the $m = 0$ modes. The steady-state curves, denoted by dashed lines, exhibit oscillations that are associated with the addition of new radial nodes to the eigenfunctions as the aspect ratio increases. As expected, these curves decrease towards the critical Rayleigh number for an unbounded layer as Γ increases. The solid curves are the Hopf curves and as before they are of two types. First there are the short segments connecting the various steady curves via TB points. In the non-rotating cylinder such Hopf curves are absent since the eigenvalues must be real (cf. Jones & Moore 1979). In addition there are Hopf curves corresponding to the oscillations that are expected because of the low Prandtl number of the fluid. These curves extend to large aspect ratios, but the corresponding critical Rayleigh numbers increase rapidly with Γ. Consequently for large Γ each oscillatory mode is preceded by the corresponding steady-state mode.

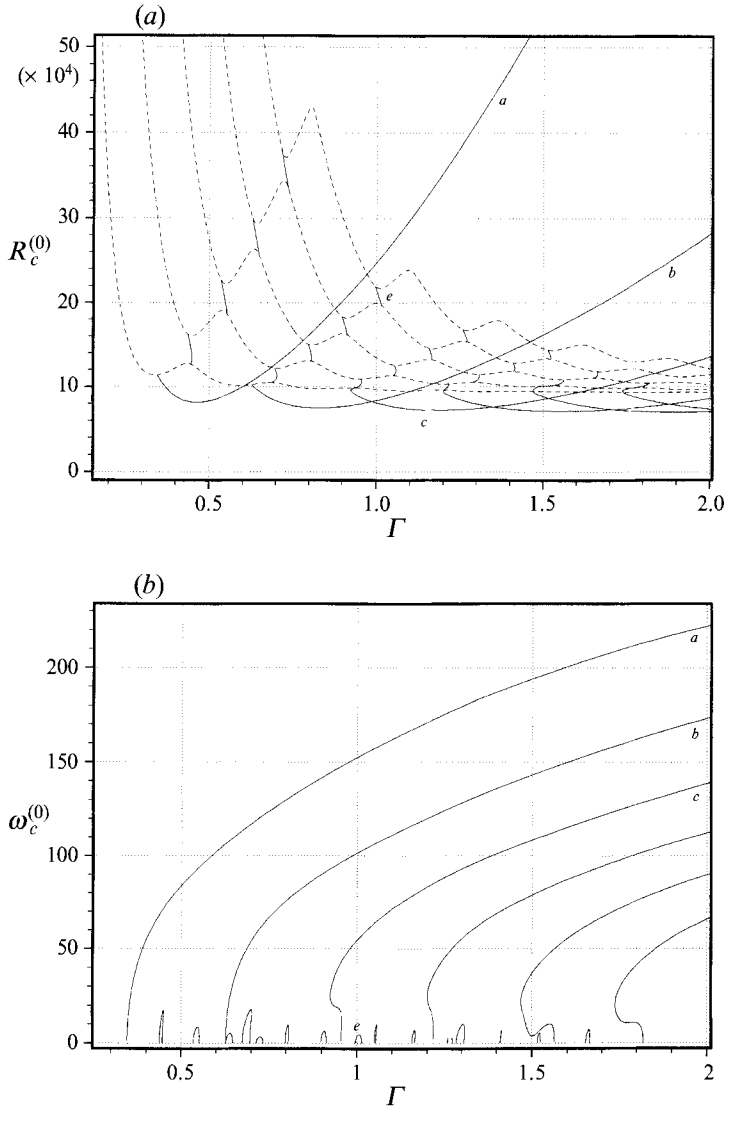

FIGURE 8. (*a*) $R_c^{(0)}$ and (*b*) $\omega_c^{(0)}$ as functions of the aspect ratio Γ for $m = 0$ modes with $\sigma = 0.49$ and $\mathscr{T} = 1000$.

With decreasing Γ the Hopf curves all terminate on steady-state curves in TB points. This is not surprising since as Γ decreases, the influence of the no-slip sidewall increases, and the boundary conditions there oppose the flow reversal that occurs during each oscillation. In consequence as Γ increases, the oscillation frequencies also increase. Note that the behaviour near the TB points varies with the aspect ratio, the Hopf curves developing a fold as Γ increases. Note also that for $\Gamma < 0.3$ the first mode to set in is a steady-state one, and that there is one additional brief interval of Γ where this occurs. For most aspect ratios, however, the onset of axisymmetric instability is via overstability. As expected, the envelope of the Hopf curves converges with increasing Γ to the critical Rayleigh number for oscillatory convection in an unbounded layer;

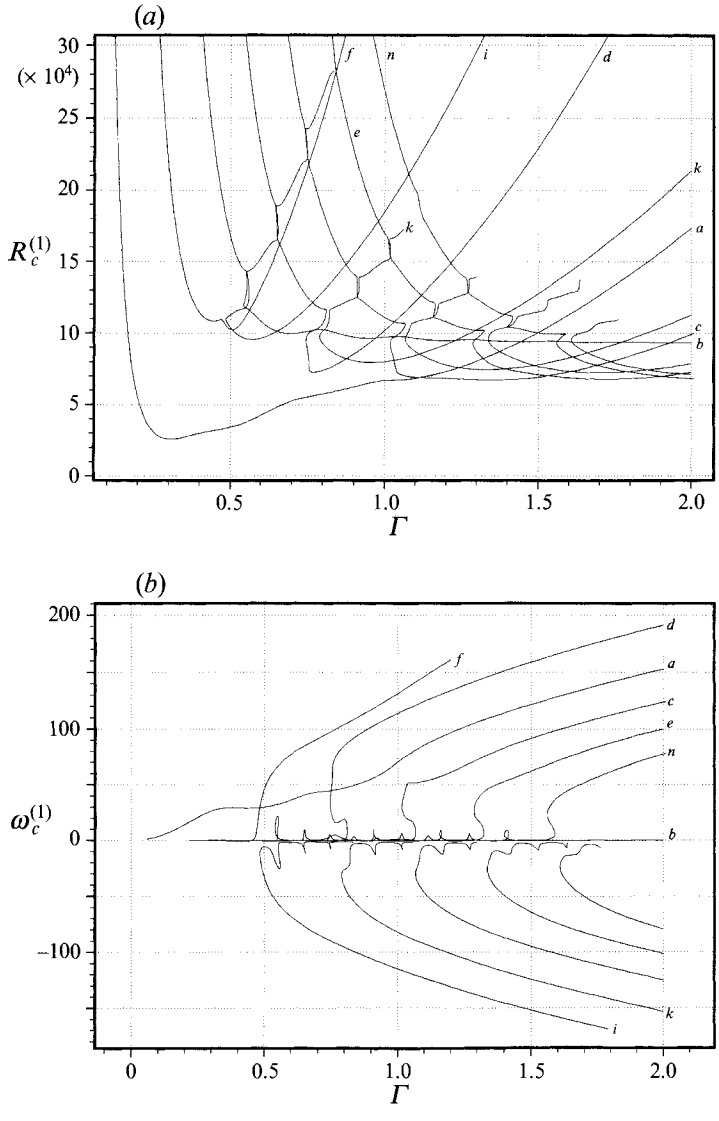

FIGURE 9. As for figure 8 but for $m = 1$.

since $\sigma < (2/3)^{\frac{1}{2}}$ this value is less than the corresponding value for steady-state instability.

In figure 9 we show the corresponding results for $m = 1$. As in the earlier cases we see here the effect of rotational splitting of the $m = 1$ modes, particularly in the short Hopf curves connecting two steady-state $m = 0$ curves. The rotational splitting results in either mode avoidance or mode crossing, with the latter typical for the higher modes. We also see the rotational splitting for the other Hopf curves arising from TB bifurcations. The most prominent feature of figure 9(*a*) is the presence of the low-lying Hopf curve once again apparently without a partner (see figure 9*b*). This curve connects smoothly to a curve that at small aspect ratios behaves like a steady-state curve. For $\Gamma < O(1)$ this curve reduces significantly the critical Rayleigh number, and inspection of the other figures identifies it as the wall mode *a*. We see that with

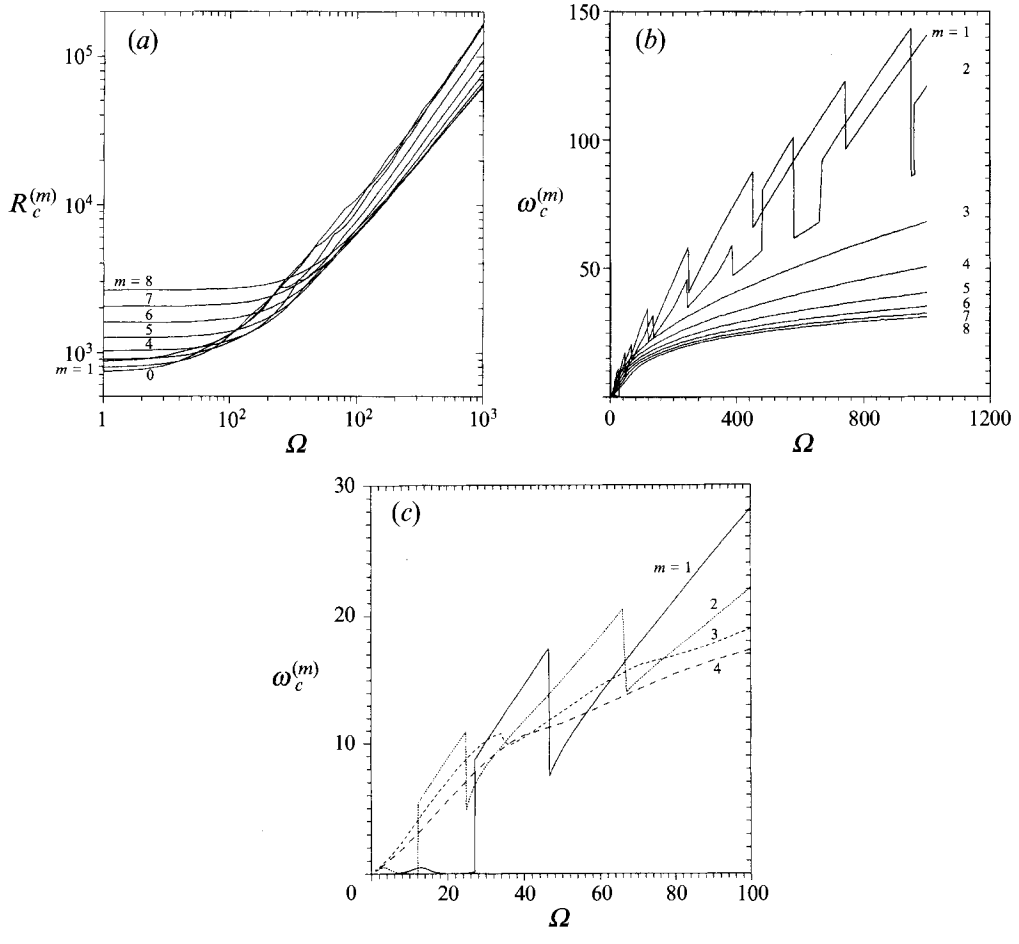

FIGURE 10. (*a*) $R_c^{(m)}$ and (*b*) $\omega_c^{(m)}$ as functions of the dimensionless rotation rate Ω for a number of values of m, and stress-free boundary conditions at top and bottom. The parameters are $\sigma = 0.49$, $\Gamma = 1.97$. The jumps in (*b*) for $m = 1$ and $m = 2$ correspond to transitions between *different* $m = 1$ and $m = 2$ modes, respectively. (*c*) Same as (*b*) but for smaller rotation rates.

increasing aspect ratio this mode is superseded by other $m = 1$ modes, first by the fifth lowest mode in figure 7(*a*), and then by others. For larger aspect ratios the critical Rayleigh numbers for the first unstable $m = 0$ and the first unstable $m = 1$ modes are nearly the same. In both cases the unstable modes are inertial.

It is worth remarking that for $\sigma = 0.49$ the $m = 0$ Hopf modes behave with increasing Γ like the non-axisymmetric wall modes discussed in Goldstein *et al.* (1993), while the steady $m = 0$ modes behave like the body modes. These two classes remain visible in the $m = 1$ results, and should be compared with the corresponding ones for $\sigma = 7.0$. Figures 8 and 9 also provide a clue as to the manner in which the short Hopf segments disappear with decreasing $\mathscr{T}$. The TB points with which the inertial oscillations terminate in figure 8(*a*) move towards larger Γ with decreasing $\mathscr{T}$ and in so doing reconnect with the nearest Hopf segment. This detaches the Hopf curve from the lowest steady-state curve and reattaches it to the next one. In this way the Hopf segments are 'swept' outwards towards larger Γ by the retreating inertial oscillations.

In figure 10 we show the results for $\sigma = 0.49$ and stress-free boundary conditions at top and bottom as a function of the rotation rate Ω for a $\Gamma = 1.97$ cylinder. The results

given below should be compared with those for $\Gamma = 1$, as well as with those for the boundary conditions B described in §5. In order to facilitate the latter comparison we present in figure 10(*a*) only the lowest value of $R_c^{(m)}$ from each value of m, thereby eliminating the multiplicity of modes with the same azimuthal wavenumber. As a consequence of this the critical Rayleigh number curves exhibit cusps near certain rotation rates, where different modes with the same m cross. Figure 10(*b*) gives the corresponding precession frequencies, while figure 10(*c*) gives more detailed information at low rotation rates. The mode crossing responsible for the cusps in figure 10(*a*) is reflected in the frequency jumps seen in figure 10(*b*, *c*). At $\sigma = 0.49$ this competition between different modes with the same azimuthal wavenumber occurs only for $m = 1$ and $m = 2$. For small rotation rates the lowest-lying $m = 1$ and $m = 2$ modes have substantially smaller precession frequencies than at larger rotation rates. This drop in the rotation frequency is related to the fact that at $\sigma = 0.49$ the axisymmetric mode oscillates only for $\Omega \geqslant 51$; for lower Ω this mode is steady. However, the corresponding $m = 1$ and $m = 2$ modes cannot be steady since they break axisymmetry. Consequently these modes do precess, albeit slowly. Note that the $m = 0$ mode is in fact preferred for $\Omega < 4$.

4. Interpretation of the results

We now turn to the interpretation of the results presented in the preceding section. We consider first the near collisions among the various modes, and then discuss the limit $\sigma \to 0$.

4.1. *Mode collisions*

In this subsection we discuss the qualitative behaviour revealed by the Prandtl- and Taylor-number dependence of the critical modes, particularly of their frequencies (see figure 2*b*). In §3 we pointed to several examples of mode interactions or near collisions that came about when the axisymmetry of the mode was broken. In this section we discuss the qualitative behaviour near such collisions and point out that it has a simple explanation. As suggested in §3 it is related to the proximity to the so-called Takens–Bogdanov bifurcation that characterizes the transition from steady to oscillatory convection for axisymmetric ($m = 0$) modes. The TB bifurcation is a codimension-two bifurcation that arises when the Hopf frequency vanishes. Consequently the bifurcation is characterized by a double zero eigenvalue. At the TB bifurcation of an $m = 0$ mode we may write any field $\psi_0(r, \phi, z)$ in the form

$$\psi_0(r, \phi, z) = u_0 f_0(r, z) + \ldots, \tag{8}$$

where the dots denote nonlinear terms, and the real amplitude u_0 satisfies

$$\begin{pmatrix} \dot{u}_0 \\ \dot{v}_0 \end{pmatrix} = \begin{pmatrix} 0 & 1 \\ 0 & 0 \end{pmatrix} \begin{pmatrix} u_0 \\ v_0 \end{pmatrix} + \ldots . \tag{9}$$

These expressions hold regardless of whether the system rotates or not. An $m \neq 0$ mode breaks the circular symmetry of the container, however, and (8) is modified. In a non-rotating cylinder one must now write

$$\psi_m(r, \phi, z) = \mathrm{Re}\{u_m f_m(r, z)\, \mathrm{e}^{\mathrm{i}m\phi}\} + \ldots, \tag{10}$$

where

$$\begin{pmatrix} \dot{u}_m \\ \dot{v}_m \end{pmatrix} = \begin{pmatrix} 0 & 1 \\ 0 & 0 \end{pmatrix} \begin{pmatrix} u_m \\ v_m \end{pmatrix} + \ldots . \tag{11}$$

Since (u_m, v_m) are now complex, the multiplicity of the zero eigenvalue has doubled. Away from the bifurcation the evolution of the amplitudes is described, without loss of generality, by

$$\begin{pmatrix} \dot{u}_m \\ \dot{v}_m \end{pmatrix} = \begin{pmatrix} 0 & 1 \\ \alpha & \beta \end{pmatrix} \begin{pmatrix} u_m \\ v_m \end{pmatrix} + \ldots, \tag{12}$$

where (α, β) are the unfolding parameters. When the system is non-rotating, these parameters are forced to be real by the reflection symmetry $\phi \to -\phi$ (Dangelmayr & Knobloch 1987). When the system rotates this reflection symmetry is absent, however, and the unfolding parameters become complex. Without loss of generality we now have

$$\begin{pmatrix} \dot{u}_m \\ \dot{v}_m \end{pmatrix} = \begin{pmatrix} 0 & 1 \\ \alpha + \mathrm{i}\Omega\gamma & \beta + \mathrm{i}\Omega\delta \end{pmatrix} \begin{pmatrix} u_m \\ v_m \end{pmatrix} + \ldots, \tag{13}$$

where α, β, γ and δ are all real functions of Ω^2. With the nonlinear terms (...) omitted (13) provides a complete description of the effects on the linear problem near a TB bifurcation of both rotation and departure from axisymmetry. By construction the equations require the presence of a TB bifurcation when the imaginary terms are absent. This can occur in one of two ways. Either there is a TB bifurcation to a non-axisymmetric mode in the non-rotating system, in which case (13) describes the effect of *rotation* on the bifurcation, or there is a TB bifurcation for an $m = 0$ mode in the rotating system, and (13) describes the effect of small *departures* from axisymmetry. In the former case $m = O(1)$ and Ω is small; in the latter it is the other way around. In the rotating convection problem the former possibility does not arise and we must therefore take γ, δ to be both $O(m)$, $m \ll 1$. Of course the geometry of the container prevents us from considering the small values of m for which the above derivation holds. Nonetheless, the resulting equation accounts for much of the behaviour seen for $m = 1$ in figure 2*b*.

To analyse the resulting linear problem we look for solutions growing as e^{st}. The growth rate s satisfies the equation

$$s^2 - (\beta + \mathrm{i}\Omega\delta)\, s - (\alpha + \mathrm{i}\Omega\gamma) = 0. \tag{14}$$

The neutral stability condition $\mathrm{Re}\, s = 0$ then yields the two relations

$$\omega^2 - \Omega\delta\omega + \alpha = 0, \quad \beta\omega + \Omega\gamma = 0, \tag{15}$$

where $\omega \equiv \mathrm{Im}\, s$. In the following we consider two cases. In the first the TB point is chosen as the point $(R_{TB}(\Omega), \sigma_{TB}(\Omega))$, so that

$$\alpha = a(\Omega)(R - R_{TB}) + b(\Omega)(\sigma - \sigma_{TB}), \quad \beta = c(\Omega)(R - R_{TB}) + d(\Omega)(\sigma - \sigma_{TB}). \tag{16}$$

In the second case σ is the parameter and the TB point is $(R_{TB}(\sigma), \Omega_{TB}(\sigma))$. Here

$$\alpha = a(\sigma)(R - R_{TB}) + b(\sigma)(\Omega - \Omega_{TB}), \quad \beta = c(\sigma)(R - R_{TB}) + d(\sigma)(\Omega - \Omega_{TB}). \tag{17}$$

To obtain results relevant to figure 2(*b*) we take σ as the distinguished bifurcation parameter and eliminate the R-dependence from (15) and (16):

$$[\omega^2 + \Delta(\sigma - \sigma_{TB})]\,\omega - \Omega\delta\omega^2 - (a/c)\,\Omega\gamma = 0. \tag{18}$$

Here $\Delta \equiv -(ad - bc)/c > 0$, so that $\omega^2 > 0$ in $\sigma - \sigma_{TB} < 0$, as in figure 1(*b*). Equation (18) will be recognized as a particular case of the universal unfolding of the pitchfork bifurcation (Golubitsky & Schaeffer 1984):

$$\omega^3 + \mu\omega + \eta\omega^2 + \nu = 0, \tag{19}$$

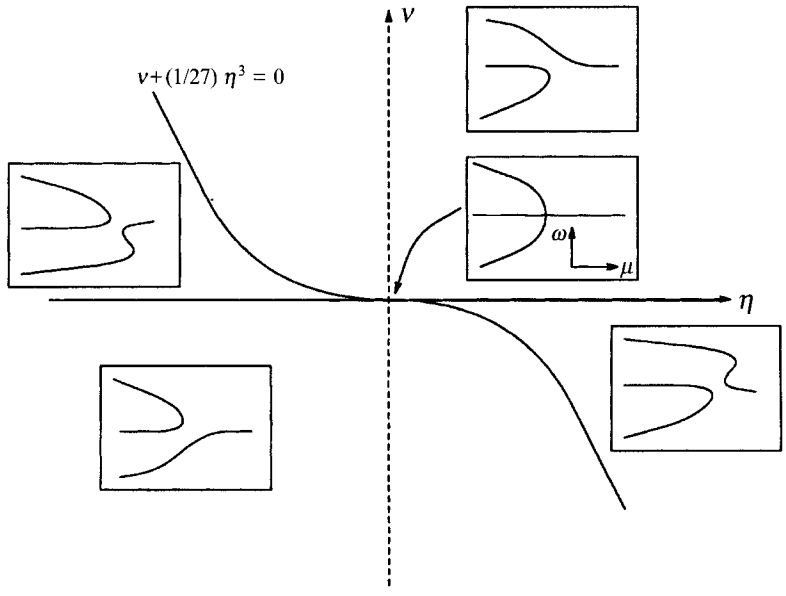

FIGURE 11. The universal unfolding (19) of the pitchfork bifurcation in the (ν, η)-plane. The unfolding describes qualitatively the generation of precession ($\omega \neq 0$) arising from the loss of axisymmetry of the pattern near a Takens–Bodganov point.

with
$$\mu = A(\sigma - \sigma_{TB}), \tag{20}$$
$$\eta = -\Omega\delta, \tag{21}$$
$$\nu = -(a/c)\Omega\gamma. \tag{22}$$

In particular, when $m = 0$ equation (18) reduces to the branching equation for the pitchfork bifurcation. Figure 11 shows how the pitchfork breaks up as a function of η and ν, and illustrates how the pitchfork produced by the coalescence of a pair of complex-conjugate eigenvalues of a *real* dispersion relation is deformed into the equivalent of an imperfect bifurcation once the dispersion relation acquires a small imaginary part. A similar observation has already been made by Soward (1979). The above discussion makes quite clear the relation between the lack of axisymmetry, and the presence of complex eigenvalues that, because of the broken symmetry, are no longer exact conjugates of one another.

In the present example the parameters η, ν are not independent, however, and increasing m corresponding to traversing the figure along the line $\nu = (a/c)(\gamma/\delta)\eta$. As the parameter Ω varies so does the slope $(a/c)(\gamma/\delta)$ of this line, and consequently the nature of the breakup of the pitchfork. Observe, however, that unless the slope is very small, the breakup will take the form of an 'imperfect' transition. In some cases, e.g. for an unbounded layer with free boundaries at top and bottom, the ratio a/c is simple to calculate (Guckenheimer & Knobloch 1983). In the present case we do not compute this ratio, but instead interpret our results in the light of the above analysis. A glance at figure 2(*c*) reveals that the 'imperfect' transition occurs only for mode interactions for which σ_{TB} is small, e.g. for *c* and *l*, or *e* and *j*. On the other hand when σ_{TB} becomes larger (i.e. the radial wavenumber becomes smaller) a 'hysteretic' transition is favoured (see e.g. modes *b* and *m* in figure 2*b*). In terms of figure 11 this behaviour has a simple explanation if a/c decreases rapidly with decreasing radial wavenumber

of the pattern. The results in the (R, Ω)-plane are similar. By analogy with the unbounded case for which $a/c = \sigma(1+2\sigma)/(1+\sigma)$, we expect for similar wavenumber modes a low Prandtl number to favour a 'hysteretic' transition in this plane. However, as in the (R, σ) analysis, it is the radial structure that appears to be responsible for the observed transitions, and the dominant transitions are 'imperfect'.

It remains to consider the nature of the near collisions in the (R, σ)- and (R, Ω)-planes. In this case we eliminate ω from (15) and obtain the equation

$$\alpha\beta^2 + \Omega^2\gamma(\gamma + \beta\delta) = 0. \tag{23}$$

Thus when $m = 0$ the interaction consists of the line $\alpha = 0$ and the half-line $\beta = 0$, $\alpha < 0$, the latter doubled. In figure 1(*a*) $\alpha = 0$ is a dashed line while $\beta = 0$ is the solid half-line that connects to it. When $m \neq 0$ these lines deform. Near $\alpha = 0$, one now has

$$\alpha = -(1/d^2)\,\gamma[\gamma + d\delta(\sigma - \sigma_{TB})](\sigma - \sigma_{TB})^{-2}. \tag{24}$$

Hence for $\sigma - \sigma_{TB} \gg 1$, $\alpha > 0$ when $d\gamma\delta < 0$ but $\alpha < 0$ when $d\gamma\delta > 0$. The opposite is the case for $\sigma = \sigma_{TB} \ll -1$. Note that $b = 0$ (since the threshold for the steady-state instability is independent of σ) and $a > 0$ (so that $\alpha < 0$ when $R - R_{TB} < 0$, as in figure 2*a*). Close to $\sigma = \sigma_{TB}$, however, $\alpha < 0$ and both segments of the curve fall below zero. It follows that the critical-Rayleigh-number curve crosses $\alpha = 0$ in $\sigma > \sigma_{TB}$ if $d\gamma\delta < 0$, or in $\sigma < \delta_{TB}$ if $d\gamma\delta > 0$. These conditions also follow from (23). Similarly the line $\beta = 0$ now becomes

$$\beta = \pm\Omega\gamma[-\Delta(\sigma - \sigma_{TB})]^{-\frac{1}{2}}, \quad |\sigma - \sigma_{TB}| \gg 1. \tag{25}$$

Since $\alpha < 0$ along $\beta = 0$, we must have $\Delta > 0$ (see figure 1*a*). It follows that for $\sigma - \sigma_{TB} \ll -1$ the double half-line splits into two lines, lying on opposite sides of the original double half-line (see figure 2*a*).

It remains to discuss the possibility of the prominent folds in the critical-Rayleigh-number curves. The formation of these requires the existence of an inflexion point, i.e. a real solution to the conditions $\mathrm{d}\sigma/\mathrm{d}R = \mathrm{d}^2\sigma/\mathrm{d}R^2 = 0$. A straightforward calculation using (23) shows that such a solution exists if and only if $d\gamma\delta < 0$. Thus the 'hysteresis' transition is associated with the crossing of $\alpha = 0$ in $\sigma > \sigma_{TB}$, as in figure 2(*a*). Note, however, that the condition $\beta = 0$ cannot be satisfied so that the critical curves cannot cross the line $\beta = 0$. In this respect the theory based on assuming that $m \ll 1$ fails when it comes to understanding the observed interaction between, for example, modes d and k. No doubt this is because in these cases the curve $\beta = 0$ acquires a negative slope near $\alpha = 0$ (cf. figure 1*a*); consequently a more complete analysis must focus on the unfolding of a degenerate pitchfork. In other respects, however, the above analysis provides a good qualitative understanding of the parameter dependence of the non-axisymmetric modes.

It is a simple matter to adapt the above analysis to describe the interactions observed in the (R_c, Ω)- and (ω_c, Ω)-planes. When $m = 0$ the modes d and i, a and k, and b and m are linked pairwise by their coalescence at their respective Ω_{TB}. In this way the 'avoided' crossings involving modes d and i, and b and m in figures 5(*a*) and 5(*b*) can readily be understood as 'imperfect' transitions caused by breaking the axisymmetry of oscillatory $m = 0$ modes. On the other hand the complete interaction between modes a and k and in particular the appearance of the loops involves the modes d and m and so cannot be understood by unfolding a single TB bifurcation. Such loops only occur in the unfolding of a double TB bifurcation formed by bringing together the two TB bifurcations at either end of one of the short segments of oscillatory modes seen in figure 4.

4.2. *The zero-Prandtl-number limit*

In order to assist in the interpretation of the small-Prandtl-number results we examined the zero-Prandtl-number limit of equations (1) and (2). As pointed out by Thual (1992) there are several ways of taking this limit. This is because the Prandtl number can be small either because the viscosity is small or because the thermal diffusivity is large. In the former case the motion is dominated by the constraint arising from the Taylor–Proudman theorem. This is the limit that is of interest in geophysical applications, and corresponds to very large Taylor numbers. In the laboratory experiments discussed in § 5 the Taylor numbers do not reach high values, however, and the more appropriate limit is that obtained by assuming that $\mathscr{T}$ remains of order one. In this case the zero-Prandtl-number limit corresponds to large thermal diffusivity (cf. Thual 1992). The resulting critical Rayleigh number will be of order one, though the temperature difference required to drive convection will have to be large. The correct scaling is to scale $\boldsymbol{u}$ with σ and the time with σ^{-1}, while the temperature fluctuation Θ scales with σ. This procedure implies that the relevant timescale of motion is now the viscous timescale, the thermal timescale being so short that temperature fluctuations equilibrate essentially instantaneously. Consequently the allowed temperature fluctuation is very small. In the limit the resulting linear equations are

$$\partial_t \boldsymbol{u} = -\nabla p + \nabla^2 \boldsymbol{u} + R\Theta\hat{\boldsymbol{z}} + \mathscr{T}\boldsymbol{u}\times\hat{\boldsymbol{z}}, \tag{26}$$

$$0 = w + \nabla^2\Theta, \tag{27}$$

$$\nabla\cdot\boldsymbol{u} = 0. \tag{28}$$

It follows that the precession velocity of non-axisymmetric patterns will be $O(\sigma)$ in the scaling leading to equations (1) and (2), or $O(1)$ in the above scaling. In dimensional terms the frequency is $O(\nu/h^2)$. This scaling is the appropriate one if one is interested in precessing patterns in slowly rotating containers in the limit of small Prandtl numbers. We have verified that the solutions to (26)–(28) are very close (i.e. $O(\sigma)$ close) to those of (1)–(3) with $\sigma = 0.025$ for slow rotation rates, the error increasing typically linearly with the rotation rate. This behaviour is expected from the scaling leading to (26)–(28).

The 'other' low-Prandtl-number limit corresponds in the scaling of (1)–(3) to the large rotation limit. In this limit the dimensional precession frequency of $O(2\Omega)$, where Ω is the dimensional rotation rate of the cylinder. In the scaling of (1)–(3) one expects the dimensionless frequencies to scale as $\sigma\mathscr{T}$. It is easy therefore to pick out from figures 4–7 those modes that persist in this limit. Note that if this limit is implemented along the lines of Soward (1977), the slowly precessing modes that arise from non-axisymmetric perturbations of the steady modes (cf. figures 5*b*, *c* and 7*b*, *c*) are eliminated. As already mentioned these modes have critical Rayleigh numbers substantially higher than the inertial modes so that the scaling appropriate to this limit does indeed focus on the relevant modes.

5. Results for rigid boundaries

We now present results for boundary conditions B and several values of the Prandtl number that are of immediate experimental interest. These results are not as complete as those for the stress-free boundaries largely because of the increased cost of the computation. The method of solution used is described by Goldstein *et al.* (1993). The results presented below are correct to 1% in the Rayleigh number and 2% in the

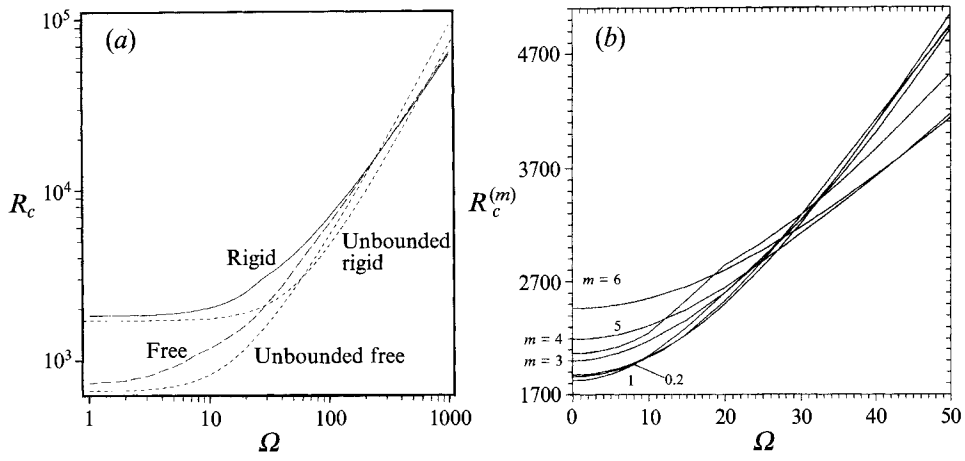

FIGURE 12. (*a*) Comparison of R_c for rigid and stress-free boundary conditions and $\sigma = 0.49$, $\Gamma = 1.97$, including the corresponding results for an unbounded layer. (*b*) $R_c^{(m)}$ for rigid boundary conditions and $\sigma = 0.49$, $\Gamma = 1.97$.

precession frequency, and focus on the smaller aspect ratios for which experiments have been done. The results are presented as a function of the dimensionless rotation rate $\Omega \equiv \frac{1}{2}\mathscr{T}$.

5.1. *Liquid ^{4}He*

The calculations reported below are motivated by the experiments of Lucas *et al.* (1983) and Pfotenhauer *et al.* (1984, 1987) on liquid ^{4}He above the λ point. The range of Prandtl numbers covered was $0.49 < \sigma < 0.76$, with the results for $\sigma = 0.49$ being the most detailed. The experiments were carried out for several aspect ratios, of which the smallest is $\Gamma = 1.97$. We begin therefore by presenting results for $\sigma = 0.49$ and $\Gamma = 1.97$.

In figure 12(*a*) we compare the critical Rayleigh numbers R_c for rigid and stress-free boundaries as a function of the dimensionless rotation rate Ω. The corresponding results for an unbounded layer have also been included. For the cylindrical container the difference between the results for the two types of boundary conditions essentially vanishes for $\Omega > 200$, much as for $\sigma = 6.8$ (Goldstein *et al.* 1993). This is not so for the unbounded layer. In both cases for sufficiently large rotation rates the rigid boundaries produce a lower critical Rayleigh number (cf. Chandrasekhar 1961). Note also that for both boundary conditions the critical Rayleigh number for the cylinder falls below that for the layer at large enough rotation rates. This is the origin of the so-called subcritical convection, observed for example by Lucas *et al.* (1983). Figure 12(*b*) shows the corresponding Rayleigh numbers $R_c^{(m)}$ for the rigid case from which figure 12(*a*) is constructed.

In figure 13(*a*) we look at these results in more detail by exhibiting the precession frequency as a function of Ω and labelling the preferred azimuthal wavenumbers. The figure distinguishes clearly between the rapidly precessing wall modes for $\Omega > 27$ (rigid case) or $\Omega > 7.5$ (stress-free case). Figure 13(*b*, *c*) shows successive enlargements of figure 13(*a*) at small Ω. Of particular interest is figure 13(*c*) which shows that for $14 < \Omega < 27$ the preferred mode in the rigid case is the non-precessing $m = 0$ mode. For yet smaller Ω the preferred modes are the slowly precessing body modes with $m = 1$ or 2.

In figure 14 we draw attention to the oscillations in the precession rate of the body modes as a function of rotation for low to moderate rotation rates. Similar oscillations

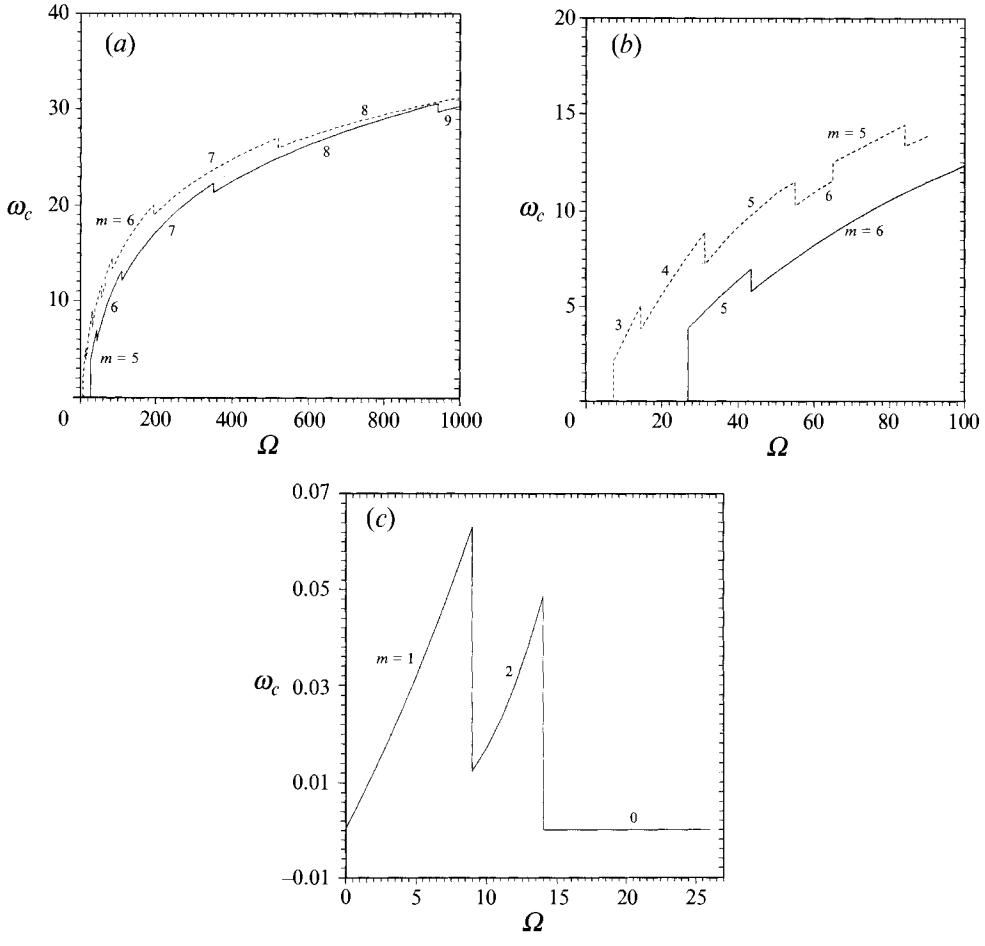

FIGURE 13. Comparison of ω_c for rigid (——) and stress-free (– – –) boundary conditions and $\sigma = 0.49$, $\Gamma = 1.97$ showing the preferred wavenumbers: (*a–c*) differ in the range of rotation rates shown.

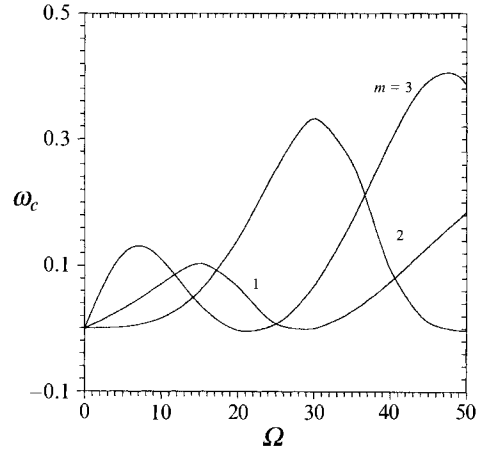

FIGURE 14. Precession frequencies $\omega_c^{(m)}$ for $m = 1, 2, 3$ for rigid boundary conditions and $\Gamma = 1.97$, $\sigma = 0.49$ showing oscillatory behaviour with increasing rotation rate Ω.

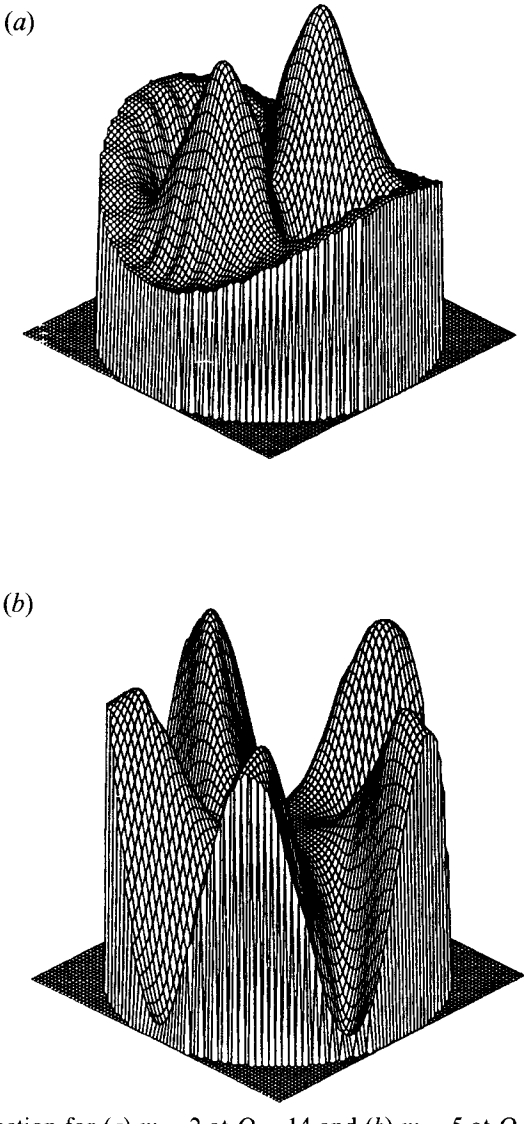

FIGURE 15. The eigenfunction for (*a*) $m = 2$ at $\Omega = 14$ and (*b*) $m = 5$ at $\Omega = 27$ for rigid boundary conditions and $\sigma = 0.49$, $\Gamma = 1.97$. The critical Rayleigh numbers are (*a*) $R_c^{(2)} = 2193$ and (*b*) $R_c^{(5)} = 2974$. The mode (*a*) is a body mode while mode (*b*) is a wall mode.

can be seen in figure 10(*c*) for stress-free boundaries, and in more detail in figure 7(*c*). These oscillations are not visible in figure 13(*c*) because the body modes are soon superseded by other body modes and then by the wall modes. Note that the prograde modes do not appear in figures 10(*c*) and 14 because their critical Rayleigh number is higher than that for the retrograde modes shown.

Typical eigenfunctions, representing the mid-level temperature fluctuation, are shown in figure 15. In figure 15(*a*) we show a body mode with $m = 2$ at $\Omega = 14$; figure 15(*b*) shows a wall mode with $m = 5$ at $\Omega = 27$. These modes are the first to set in as the Rayleigh number increases at the given rotation rates. Note that for rigid boundaries the situation resembles that for free boundaries at somewhat higher Prandtl numbers. This is to be expected since rigid boundaries decrease the maximum Prandtl number at which a particular axisymmetric mode will oscillate, for a given rotation rate.

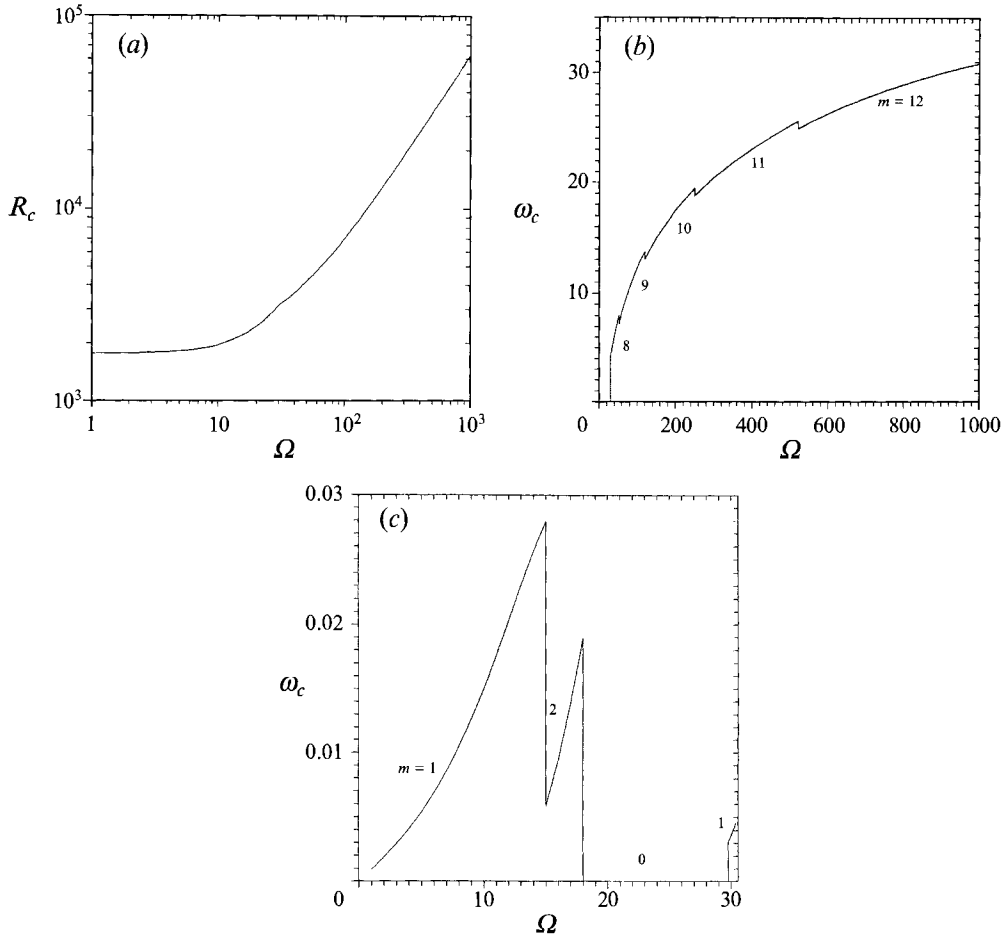

FIGURE 16. (*a*) The critical Rayleigh number R_c for rigid boundaries and $\sigma = 0.525$, $\Gamma = 2.8$ as a function of the rotation rate. (*b*, *c*) The corresponding precession frequencies ω_c on different scales for Ω.

In figure 16 we present results for $\sigma = 0.525$ and $\Gamma = 2.8$. We find that the mode $m = 1$ is preferred for $0 < \Omega < 15$, followed by $m = 2$ in $15 < \Omega < 18$, $m = 0$ in $18 < \Omega < 30$, $m = 1$ in $30 < \Omega < 31$, with a transition to a fast $m = 8$ mode at $\Omega = 31$.

5.2. *Mercury*

Extensive experiments on convection in mercury ($\sigma = 0.025$) have been reported by Rossby (1969). These were performed in a relatively large aspect ratio container (the aspect ratio is not specified) and typically at large rotation rates. We have computed R_c and the corresponding Hopf frequency ω_c for this case as functions of the rotation rate for a $\Gamma = 1$ container (figure 17). With rigid boundaries the mode $m = 0$ is preferred in the interval $0 < \Omega < 16$ and is then steady; in the interval $16 \leqslant \Omega \leqslant 681$ the preferred mode is $m = 2$, with $m = 3$ preferred for yet larger rotation rates. The oscillatory $m = 0$ modes are always preceded by other modes. In contrast, with the boundary conditions A the mode that first sets in is $m = 1$ in the interval $0 < \Omega < 345$, followed by $m = 2$ in $346 < \Omega < 910$ and $m = 3$ for higher Ω (see figure 17*b*). Consequently, the detailed study of the various competing $m = 1$ modes carried out in §3 is relevant for a substantial range of rotation rates. For Prandtl numbers this low

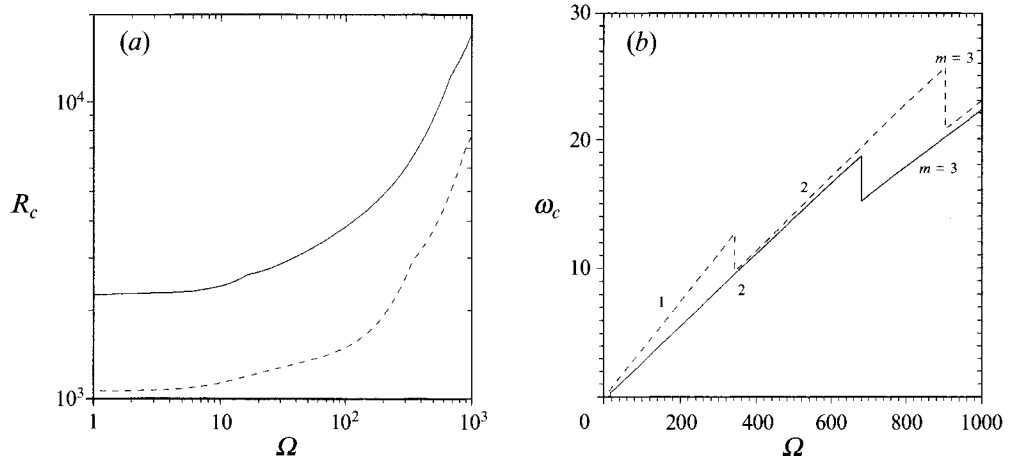

FIGURE 17. Comparison of (*a*) R_c and (*b*) ω_c between rigid (——) and stress-free (– – –) boundary conditions for $\sigma = 0.025$, $\Gamma = 1.0$.

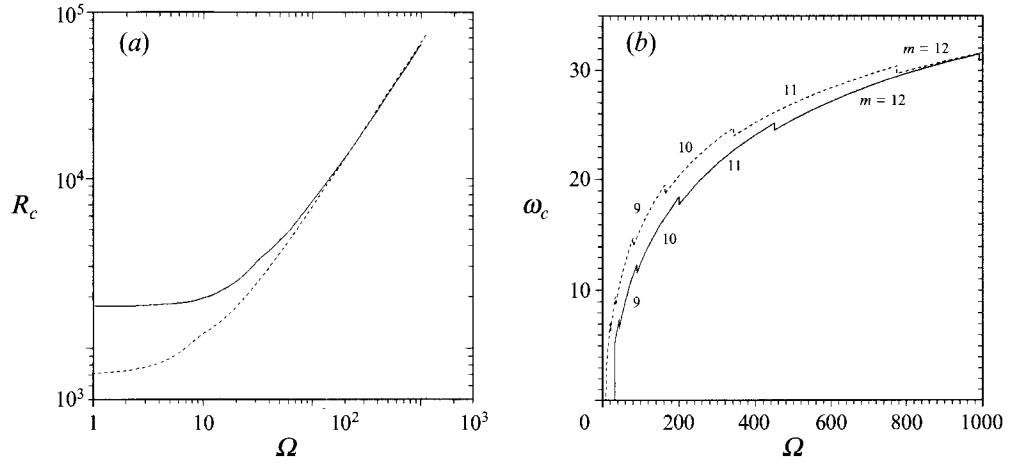

FIGURE 18. As for figure 17, but with $\sigma = 0.78$, $\Gamma = 2.8$.

the critical Rayleigh numbers for the rigid and stress-free boundary conditions continue to differ significantly for all $0 < \Omega < 10^3$ in contrast to the situation at higher Prandtl numbers (cf. figure 12*a*; see also Goldstein *et al.* 1993). This is consistent with the difference between the two varying as $(\sigma\mathscr{T})^{-\frac{1}{6}}$, the result for an unbounded layer (Clune & Knobloch 1993).

5.3. *Compressed CO_2 gas*

Detailed experiments on convection in compressed CO_2 gas have been performed recently by G. Ahlers and coworkers (Y. Hu, R. Ecke & G. Ahlers, unpublished). In this system the Prandtl number can be varied by changing the pressure in the cell. Existing experiments have been carried out for $\sigma = 0.80$. Although this Prandtl number is too large for overstability, our results are of immediate relevance not only to the compressed gas experiments but also to liquid helium experiments at the upper end of the accessible Prandtl numbers ($\sigma = 0.76$). We use the latter experiment as motivation for choosing $\sigma = 0.78$ and $\Gamma = 2.8$. The results are summarized in figure 18. These are similar to both the higher-Prandtl-number results discussed by Goldstein *et al.* (1993) and the $\sigma = 0.525$ results presented above. For the boundary conditions B

one first finds an $m = 1$ mode, followed at $\Omega = 15$ by $m = 2$. This mode is superseded by an $m = 0$ mode at $\Omega = 18$. The $m = 1$ mode comes in at $\Omega = 30$ followed by a jump to a fast $m = 8$ mode at $\Omega = 33$. At $\Omega = 44$ this is superseded by $m = 9$ with jumps to $m = 10, \ldots, 13$ taking place at $\Omega = 90$, 200, 450 and 990, respectively.

5.4. *Comparison with experiments*

Most low-Prandtl-number experiments are cryogenic, and hence suffer from the disadvantage that the flow cannot be visualized. Consequently the onset of instability is determined only through integrated measurements such as Nusselt-number measurements. Such measurement cannot, however, distinguish between a steadily precessing pattern or a steady one, since the Nusselt number is constant in both cases. In particular, existing experiments do not provide information about either the precession frequencies or the mode numbers. Consequently the scope for detailed comparison to experiments is more limited than for moderate-Prandtl-number experiments. Nonetheless, in order to facilitate such a comparison both to currently available and future data the results presented in §§5.1–5.3 emphasize calculations with experimental boundary conditions. We have focused on the case $\sigma = 0.49$, $\Gamma = 1.97$ for which the currently available data are most complete (Pfotenhauer *et al.* 1987). We have not presented results for the larger aspect ratios investigated by Pfotenhauer *et al.* (1984) because the number of modes close to critical becomes large, and the weakly nonlinear problem is then unlikely to be dominated by a single linear theory mode. We have also focused on the case $\sigma = 0.525$, $\Gamma = 2.8$ because of recent experiments on normal binary ^{3}He–^{4}He mixtures reported by Thurlow (1993). At the highest temperature at which these experiments were carried out this system corresponds fairly closely to a pure ^{4}He fluid with σ near 0.525. The critical-Rayleigh-number data reveal a prominent cusp at $\Omega = 355$ while our calculations reveal cusps near $\Omega = 250$ and $\Omega = 520$ associated, respectively, with the transition from $m = 10$ to $m = 11$ and $m = 11$ to $m = 12$. Whether the presence of such cusps can be used to identify the azimuthal wavenumbers of the unstable modes in the experiment remains unclear. Evidently local probes, as used in the recent experiments of Zhong *et al.* (1991, 1993), would provide an invaluable diagnostic tool.

The experiments of Pfotenhauer *et al.* (1984, 1987) reveal that for sufficiently large rotation the critical Rayleigh number $R_c(\Omega)$ falls below that for an unbounded layer, hereafter $R_\infty(\Omega)$. This 'subcritical' convection is characterized by lower heat transport efficiency, as revealed by the Nusselt-number measurements, than the convection for $R > R_\infty(\Omega)$. Consequently, the Nusselt-number curves $N(R)$ exhibit an unambiguous break at about $R_\infty(\Omega)$, beyond which the slope $\mathrm{d}N/\mathrm{d}R$ becomes significantly larger than for $R < R_\infty(\Omega)$. For example, for $\Gamma = 7.81$ and $\sigma = 0.49$ the break is present whenever $\Omega > 140$. These observations are consistent with our prediction that for sufficiently large rotation rates, $\Omega > 26$ for $\Gamma = 1.97$, $\sigma = 0.49$, the instability will take the form of wall modes, much as for $\sigma = 6.8$ (Goldstein *et al.* 1993). The wall modes set in at substantially lower values of the Rayleigh number than the $m = 0$ mode whose threshold is approximated the best by the results for an unbounded layer used in their interpretation (cf. figure 12*b*). In this sense the presence of the walls is *destabilizing*. In addition the wall modes precess rigidly, and hence produce a time-independent Nusselt number. The break in the Nusselt-number slope is likely to arise from an instability to the body modes at higher Rayleigh numbers. These modes have a non-zero amplitude throughout the container and hence are much more efficient at heat transport than the wall modes. Moreover they are first excited precisely near $R_\infty(\Omega)$. Indeed Zhong *et al.* (1993) have seen the centre of their container 'fill in' abruptly with increasing Rayleigh

number, and attributed this to the appearance of a new mode of instability. Similar breaks in the Nusselt number have also been observed by Thurlow (1993) and a similar interpretation applies to his results as well as to those of Rossby (1969). Our calculations present a number of quantitative predictions for low-Prandtl experiments that should prove invaluable when flow visualization finally becomes available.

6. Discussion

The results of this paper show that the linear stability problem for the conduction state in a rotating cylinder becomes much more complicated for small Prandtl numbers than is the case for moderate Prandtl numbers (Goldstein *et al.* 1993). In particular, the multiplicity of modes relevant at low Prandtl numbers can be quite large, and the transitions among them as the Prandtl number or rotation rate are varied can be exceedingly complex. Like the modes considered by Goldstein *et al.* all the modes discussed in this paper have the simplest possible structure in the vertical direction; they differ only in their radial structure, both with respect to the number of radial 'nodes' and the behaviour near the sidewall. This characterization in terms of 'nodes' is, however, imprecise, since the pure radial modes are coupled through the boundary conditions. The modes discussed all have a radial structure that minimizes or nearly minimizes the Rayleigh number; no radial overtones are included. We have attempted to classify these modes into wall and body modes, a terminology that proved both useful and unambiguous for moderate or large Prandtl numbers. At low Prandtl numbers we have found that this distinction fails, since for fixed rotation rate a mode that is a wall mode at moderate Prandtl numbers metamorphoses into a body mode at low Prandtl numbers. Here the term body mode continues to imply that the eigenfunction fills the container and peaks near the centre.

The mode classification is further complicated by the fact that there are two types of inertial modes, the wall modes known at larger Prandtl numbers and oscillatory modes present for low Prandtl numbers. In both cases it is the Coriolis force that is responsible for the presence of the modes. The former exist only in a bounded container, while the latter are properly viewed as body modes since they exist even in the absence of a sidewall. With decreasing Prandtl number both the wall modes and the body modes described by Goldstein *et al.* (1993) become inertial body modes. In terms of our non-dimensionalization the frequency of these oscillations is of order $\sigma\mathscr{T}$, or equivalently of order 2Ω, where Ω is now the dimensional angular velocity of the cylinder. Figure 2 shows that at low Prandtl numbers not all modes have a frequency of this order, however. There are slowly precessing modes produced through non-axisymmetric perturbations of steady axisymmetric modes that are present even at small Prandtl numbers. All these modes have higher critical Rayleigh numbers, however, than the corresponding inertial modes.

We have seen that the first unstable mode is very sensitive to the Prandtl number, although the modal structure remains similar to that at larger Prandtl numbers. As the rotation rate decreases some modes are continuously connected to those of a non-rotating cylinder, while others turn around towards larger rotation rates, often through a remarkably tortuous process. The modes that turn around clearly owe their existence to the rotation, but their connection to the inertial modes identified by varying the Prandtl number is not simple. This is due to a phenomenon discovered by Jones (1988), who pointed out that in problems of this type tracking a mode around a closed path in parameter space (here the σ, $\mathscr{T}$ space, for example) does not necessarily restore the mode to the original one. This behaviour is related to the presence of multiple

eigenvalues of the linear stability problem in the manner discussed by Jones. We have been able to uncover this wealth of behaviour only by focusing on the problem with idealized boundary conditions at the top and bottom. The complexity we have discovered must, however, be borne in mind when attempting to solve similar problems, and in particular the present problem with more realistic boundary conditions. Consequently the structure visible in the results for these boundary conditions must be attributed to the type of behaviour we have uncovered with the simpler boundary conditions.

The problem studied in this paper is a prototype of a large class of problems in which broken reflection symmetry plays a significant role. For axisymmetric disturbances the eigenvalue problem is real and eigenvalues occur in complex-conjugate pairs. When non-axisymmetric disturbances are admitted the linear operator becomes complex; complex eigenvalues are now generic and no longer occur in conjugate pairs. It is this mathematical property of the linear stability problem that is responsible for the prevalence of precessing patterns in rotating systems. We have used this observation to explain a number of qualitative features of our results by focusing on the proximity of the various Takens–Bogdanov bifurcations present in the axisymmetric state. Vestiges of these bifurcations can be seen in figures 2, 5 and 7. Arguments such as these should also prove useful for understanding the dynamics of these modes in the weakly nonlinear regime.

It comes therefore as no surprise that a number of our results bear a qualitative resemblance to those obtained by Zhang & Busse (1987) for the onset of convection in rotating spheres. The two problems have the same symmetry properties, and the arguments based on the breakup of the TB bifurcation with departures from axisymmetry holds for this system as well. In particular Zhang & Busse also find 'imperfect' and 'hysteretic' interactions among non-axisymmetric modes. In addition, however, they find a new type of transition which they refer to as a 'switch-over'. At this transition two modes of the same azimuthal wavenumber have identical but non-zero frequencies. Such an interaction is also a codimension-two bifurcation, the non-semisimple double Hopf bifurcation. Zhang & Busse (1987) find that this bifurcation is instrumental in producing a switch from a retrograde mode to a prograde mode with the same azimuthal wavenumber as the Prandtl number is decreased. We note, finally, that similar behaviour also arises in compressible magnetoconvection in an inclined magnetic field (Matthews *et al.* 1992). In this example the 'hysteresis' diagrams were not observed. This is because their presence is typically accessible only when a second symmetry-breaking effect (e.g. rotation) is present.

The work at Berkeley was supported by an INCOR grant from Los Alamos National Laboratory and was completed while E.K. was visiting the Isaac Newton Institute for Mathematical Sciences in Cambridge, UK. The work in Barcelona was supported by DGYCIT under grant PB91-0595. We have benefitted from discussions with S. Friedlander, P. Lucas, M. Rieutord and K. Zhang.

REFERENCES

BESTEHORN, M., FANTZ, M., FRIEDRICH, R., HAKEN, H. & PÉREZ-GARCÍA, C. 1992 Spiral patterns in thermal convection. *Z. Phys.* B **88**, 93–94.

BUELL, J. C. & CATTON, I. 1983 Effect of rotation on the stability of a bounded cylindrical layer of fluid heated from below. *Phys. Fluids* **26**, 892–896.

CHANDRASEKHAR, S. 1961 *Hydrodynamic and Hydromagnetic Stability*. Dover.

CLUNE, T. & KNOBLOCH, E. 1993 Pattern selection in rotating convection with experimental boundary conditions. *Phys. Rev.* E **47**, 2536–2550.

DA COSTA, L. N., KNOBLOCH, E. & WEISS, N. O. 1981 Oscillations in double-diffusive convection. *J. Fluid Mech.* **109**, 25–43.

DANGELMAYR, G. & KNOBLOCH, E. 1987 The Takens–Bogdanov bifurcation with $O(2)$ symmetry. *Phil. Trans. R. Soc. Lond.* A **322**, 243–279.

ECKE, R. E., ZHONG, F. & KNOBLOCH, E. 1992 Hopf bifurcation with broken reflection symmetry in rotating Rayleigh–Bénard convection. *Europhys. Lett.* **19**, 177–182.

GOLDSTEIN, H. F., KNOBLOCH, E., MERCADER, I. & NET, M. 1993 Convection in a rotating cylinder. Part 1. Linear theory for moderate Prandtl numbers. *J. Fluid Mech.* **248**, 583–604.

GOLUBITSKY, M. & SCHAEFFER, D. 1984 *Singularities and Groups in Bifurcation Theory*, Vol. 1. Springer.

GUCKENHEIMER, J. & KNOBLOCH, E. 1983 Nonlinear convection in a rotating layer: amplitude expansions and normal forms. *Geophys. Astrophys. Fluid Dyn.* **23**, 247–272.

JONES, C. A. 1988 Multiple eigenvalues and mode classification in plane Poiseuille flow. *Q. J. Mech. appl. Maths* **41**, 363–382.

JONES, C. A. & MOORE, D. R. 1979 The stability of axisymmetric convection. *Geophys. Astrophys. Fluid Dyn.* **11**, 245–270.

KNOBLOCH, E. 1992 Bifurcations in rotating systems. In *Theory of Solar and Planetary Dynamos: Introductory Lectures* (ed. M. R. E. Proctor & A. D. Gilbert). Cambridge University Press, in press.

LUCAS, P. G. J., PFOTENHAUER, J. M. & DONNELLY, R. J. 1983 Stability and heat transfer in rotating cryogens. Part 1. Influence of rotation on the onset of convection in liquid ^{4}Helium. *J. Fluid Mech.* **129**, 251–264.

MARQUÉS, F., NET, M., MASSAGUER, J. M. & MERCADER, I. 1993 Thermal convection in vertical cylinders: A method based on potentials of velocity. *Comput. Math. Appl. Mech. Engng*, in press.

MATTHEWS, P. C., HURLBURT, N. E., PROCTOR, M. R. E. & BROWNJOHN, D. P. 1992 Compressible magnetoconvection in oblique fields: linearized theory and simple nonlinear models. *J. Fluid Mech.* **240**, 559–569.

PFOTENHAUER, J. M., LUCAS, P. G. J. & DONNELLY, R. J. 1984 Stability and heat transfer of rotating cryogens. Part 2. Effects of rotation on heat-transfer properties of convection in liquid ^{4}Helium. *J. Fluid Mech.* **145**, 239–252.

PFOTENHAUER, J. M., NIEMELA, J. J. & DONNELLY, R. J. 1987 Stability and heat transfer of rotating cryogens. Part 3. Effects of finite cylindrical geometry and rotation on the onset of convection. *J. Fluid Mech.* **175**, 85–96.

ROSSBY, H. T. 1969 A study of Bénard convection with and without rotation. *J. Fluid Mech.* **36**, 309–335.

SOWARD, A. M. 1977 On the finite amplitude thermal instability of a rapidly rotating fluid sphere. *Geophys. Astrophys. Fluid Dyn.* **9**, 19–74.

SOWARD, A. M. 1979 Thermal and magnetically driven convection in a rapidly rotating fluid layer. *J. Fluid Mech.* **90**, 669–684.

THUAL, O. 1992 Zero-Prandtl-number convection. *J. Fluid Mech.* **240**, 229–258.

THURLOW, M. S. 1993 Rayleigh–Bénard convection in a rotating liquid ^{3}He–^{4}He mixture: the effects of Coriolis forces and a finite geometry. PhD thesis, University of Manchester.

ZHANG, K.-K. & BUSSE, F. H. 1987 On the onset of convection in rotating spherical shells. *Geophys. Astrophys. Fluid Dyn.* **39**, 119–147.

ZHONG, F., ECKE, R. E. & STEINBERG, V. 1991 Asymmetric modes and the transition to vortex structures in rotating Rayleigh–Bénard convection. *Phys. Rev. Lett.* **67**, 2473–2476.

ZHONG, F., ECKE, R. E. & STEINBERG, V. 1993 Rotating Rayleigh–Bénard convection: asymmetric modes and vortex states. *J. Fluid Mech.* **249**, 135–159.